

Boron-induced microstructural manipulation of titanium and titanium alloys in additive manufacturing

A. Sola & A. Trinchi

To cite this article: A. Sola & A. Trinchi (2023) Boron-induced microstructural manipulation of titanium and titanium alloys in additive manufacturing, *Virtual and Physical Prototyping*, 18:1, e2230467, DOI: [10.1080/17452759.2023.2230467](https://doi.org/10.1080/17452759.2023.2230467)

To link to this article: <https://doi.org/10.1080/17452759.2023.2230467>



© 2023 The Author(s). Published by Informa UK Limited, trading as Taylor & Francis Group



Published online: 30 Aug 2023.



Submit your article to this journal [↗](#)



Article views: 1107



View related articles [↗](#)



View Crossmark data [↗](#)

Boron-induced microstructural manipulation of titanium and titanium alloys in additive manufacturing

A. Sola  and A. Trinchi 

Advanced Materials and Processing, Manufacturing Business Unit, Commonwealth Scientific and Industrial Research Organisation (CSIRO), Clayton – Melbourne, Australia

ABSTRACT

While the role of boron (B) has been thoroughly clarified in titanium (Ti) castings, the microstructural changes triggered in additive manufacturing (AM) are still the subject of debate in the literature. Many contributions have confirmed the B-induced microstructural refinement in Ti-based AM parts. The formation of TiB in titanium matrix composites (TMCs) may increase strength. In some cases, B may also promote the columnar-to-equiaxed transition, thus mitigating the anisotropic effects associated with the strong epitaxial growth of unidirectional columnar grains typical of AM. However, as critically discussed in this review, some pitfalls remain. Due to fast cooling, the microstructural evolution in AM may deviate from equilibrium, leading to a shift of the Ti-B eutectic point and to the formation of out-of-equilibrium phases. Additionally, the growth of TiB may undermine the ductility and the crack propagation resistance of AM parts, which calls for appropriate remediation strategies.

ARTICLE HISTORY

Received 18 May 2023
Accepted 23 June 2023

KEYWORDS



Boron; titanium; additive manufacturing; grain refinement; columnar growth

1. Introduction

Being a mouldless technology, additive manufacturing (AM) offers unprecedented possibilities for customisation of part's geometries in high-tech industries like aerospace, aviation, and biomedicine. Meanwhile, titanium (Ti) features an outstanding specific strength, largely originating from its low density as compared to structural metals like steel. The strength of Ti, as well as its stability and oxidation resistance, can be enhanced by the addition of elements such as aluminium (Al), oxygen (O), nitrogen (N), and carbon (C) (α stabilising elements), or molybdenum (Mo), vanadium (V), and tantalum (Ta) (β stabilising elements) to produce a variety of Ti-based alloys, which are classified as α , $\alpha+\beta$, and β alloys depending on the crystal lattice at room temperature [1]. The combination of Ti and its alloys with AM enables the production of lightweight structures, which is fundamental for reducing fuel consumption in vehicles, and for providing physiological comfort in biomedical applications [2].

In spite of the advantages coming from the AM of Ti and Ti alloys, some key challenges still exist. Due to the layer-wise build-up mechanism that underpins metal AM technologies (including direct(ed) energy

deposition (DED) [3], powder bed fusion (PBF) [4], and wire-arc AM (WAAM), which is a sub-set of DED where a wire-based feedstock is processed with an electric or plasma arc [5], as exemplified in Figure 1), a strong thermal gradient is established along the growth direction ('z' axis in Figure 1) while printing. As a consequence of directional cooling and steep thermal gradients, the microstructure of Ti-based parts is commonly characterised by significant columnar growth of β grains in the build direction [6]. Upon cooling below the ' β transus' temperature, if not stabilised, the primary β phase (body-centred cubic, bcc, structure, shown in Figure 2a, where the lattice parameters are taken from the contribution by Han et al. [7]) transitions to the α phase (hexagonal close-packed, hpc, structure, Figure 2b). In this solid-state phase transformation, the growth of grain boundary α and other α morphologies is often templated by the parent β grains ('prior- β ' grains) through orientation relationships [8]. This typically results in additively manufactured Ti and Ti alloy parts having a strong texture, which ultimately leads to anisotropic mechanical properties. For instance, the presence of grain boundary α phase that follows the columnar prior- β grain morphology serves as a

CONTACT A. Sola  antonella.sola@csiro.au  Advanced Materials and Processing, Manufacturing Business Unit, Commonwealth Scientific and Industrial Research Organisation (CSIRO), Clayton – Melbourne, VIC, Australia

© 2023 The Author(s). Published by Informa UK Limited, trading as Taylor & Francis Group
This is an Open Access article distributed under the terms of the Creative Commons Attribution-NonCommercial License (<http://creativecommons.org/licenses/by-nc/4.0/>), which permits unrestricted non-commercial use, distribution, and reproduction in any medium, provided the original work is properly cited. The terms on which this article has been published allow the posting of the Accepted Manuscript in a repository by the author(s) or with their consent.

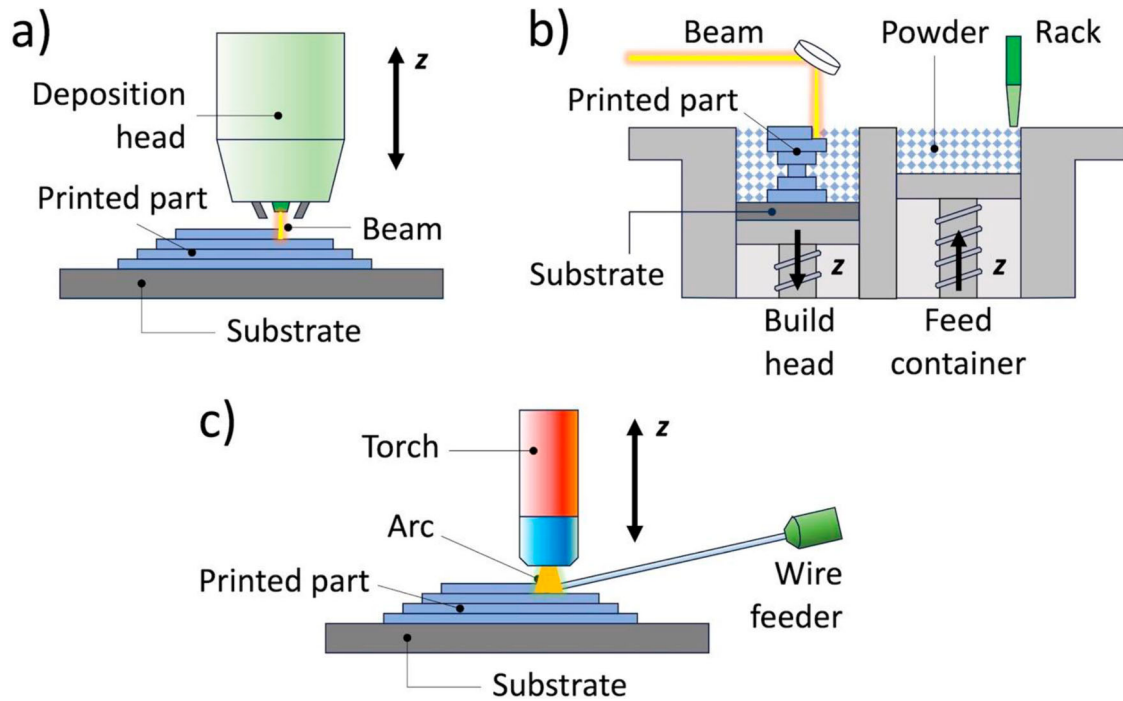


Figure 1. Illustration of common metal AM techniques where the addition of B has been explored for the manipulation of Ti and Ti alloy microstructure: (a) DED, (b) PBF, and (c) WAAM.

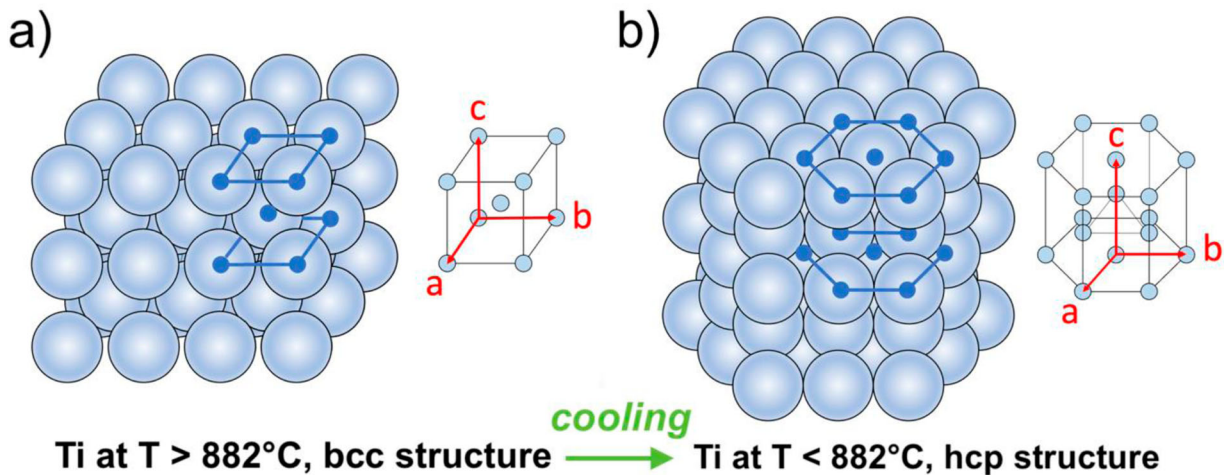


Figure 2. Lattice structure of Ti (a) above and (b) below the β -transus temperature of 882°C . Lattice parameters are $a = b = c = 0.332$ nm for the bcc structure, and $a = b = 0.295$ nm, $c = 0.468$ for the hcp structure (lattice parameters from the contribution by Han et al. [7]).

preferential path for crack propagation, leading to premature failure [9]. Accordingly, the ductility under tensile load is typically much lower in the transverse direction (i.e. normal to the growth direction) than in the longitudinal one (i.e. parallel to the growth direction) [10]. Based on literature results, Zhang et al. [11] also pointed out that large columnar β grains produce anisotropic effects in the fatigue crack propagation rate due to the preferred crack propagation along grain boundaries. Moreover, grain growth is promoted by repeated reheating, while new layers are being added on top of the previous ones, thus leading to coarse grain morphologies

[6]. This may also be detrimental to several mechanical properties. For example, even if coarse microstructures are likely to attain a higher toughness and a higher fatigue crack growth threshold thanks to the tortuosity of the crack tip associated with larger grains, the unnotched fatigue behaviour is likely much higher in fine-grained materials than in coarse-grained ones [12]. Similarly, large prior- β grains favour the development of large α colonies (i.e. 'groups' of neighbouring α laths (lamellae) having the same orientation), where the tensile strength of Ti is inversely proportional to the α colony size [13].

Two strategies have been proposed to improve the microstructural homogeneity, which rely on the promotion of a less textured β grain microstructure through the columnar-to-equiaxed (CTE) transition, or the manipulation of the α phase to induce grain refinement and suppression of unwanted variants such as grain boundary α or large colony α [14]. Drawing on the extensive knowledge historically acquired with Ti and Ti alloy casting, research is being geared towards controlling the microstructure of AM parts through the addition of trace elements such as boron, silicon, and beryllium. Among them, boron (B) is known to be an excellent grain refiner for Ti and its alloys [15], owing to its unparalleled capacity to promote constitutional undercooling and grain restriction [16,17]. B is also very effective in avoiding unfavourable α variants, to the point that adding B by 1000 ppm may be enough to eliminate grain boundary α in Ti-6Al-4V casting [18].

Besides B-driven grain refinement and texture weakening, the reactions occurring between B and Ti produce non-oxide (intermetallic) phases, such as TiB and TiB₂, which are refractory materials having high stiffness (Young's modulus) and excellent thermal stability [19,20]. Boride-reinforced Ti-matrix composites (TMCs – for the convenience of discussion, in the following the same term 'TMC' will be applied both to Ti-matrix composites and to Ti-alloy-matrix composites) offer attractive properties, such as enhanced strength and hardness [21]. TiB-reinforced TMCs also feature improved creep resistance, because the thermally stable TiB particles restrain the plastic flow of grain and/or phase boundaries at high temperature. If grown in-situ within individual Ti grains, TiB precipitates may also limit the mean free path of mobile dislocations [22]. The increased creep resistance largely relies on the achievement of a uniform dispersion of TiB in the metal matrix [21]. The creep tests conducted by Zhou et al. [23] on PBF-LB parts confirmed that the creep resistance of Ti-6Al-4V could be ameliorated through the addition of just 1.18 wt.% of TiB₂ (nominally leading to the formation of 2 vol.% of TiB), and further improvement could be achieved after heat treatment of the printed parts, because the increased α/β interfaces acted as obstacles to dislocation motion.

Among other reinforcements, TiB has received particular interest, since its addition increases oxidation resistance [19] and remediates the poor wear performance of Ti [24]. Eutectic TiB is known to grow as single-crystal nanowhiskers in the Ti matrix and, thanks to its elongated needle-like morphology, TiB exerts a strong reinforcing effect, such that a relatively small amount of TiB can significantly increase the stiffness and the surface properties (e.g. wear resistance) of Ti [25–28].

Acicular reinforcements can also contribute to toughening the composite through crack bridging [29]. TiB is thermodynamically stable in Ti [30], and its presence restricts the grain growth at high temperature, even above the β transus [31]. Closely matching the thermal expansion coefficients ($8.2 \times 10^{-6} \text{ }^\circ\text{C}^{-1}$ for Ti and $7.2 \times 10^{-6} \text{ }^\circ\text{C}^{-1}$ for TiB [29]) substantially mitigates the residual stresses at the Ti-TiB interface [24,28]. Moreover, since the densities are also similar (4.506 g/cm^3 for cp-Ti and 4.58 g/cm^3 for TiB [30,32]), TiB improves the stiffness and strength of Ti and Ti alloys without adding weight, and this provides significant weight saving benefits over the neat metal/alloy [31]. Taking into consideration the widespread adoption of Ti and its alloys in biomedical applications, another key advantage is that TiB-reinforced TMCs are biocompatible as demonstrated by *in-vitro* tests [32–34]. Electrochemical tests proved that TiB-reinforced TMCs produced by PBF-LB had better corrosion resistance than neat cp-Ti counterparts in Hank's solution. This behaviour was due to TiB and TiB₂ phases acting as micro-cathodes uniformly distributed in the Ti matrix. While anodic dissolution of Ti is prevailing in early stages of the corrosion process, rapid passivation occurs on the surface, thus leading to superior corrosion resistance [35].

Owing to the exceptional chemical and thermal stability of TiB in the Ti matrix [20], in principle TiB-reinforced TMCs can be fabricated both ex-situ and in-situ. While the ex-situ approach has been successfully demonstrated with conventional routes, such as blending raw Ti powders with TiB particles and then processing them by powder metallurgy methods [36], the in-situ approach is most commonly seen in AM. In-situ grown reinforcements have a clean interface with the surrounding matrix, which favours the establishment of strong interfacial bonding [29,37]. Conversely, contaminants are often present at the interface in ex-situ composites, which is expected to weaken the interfacial bonding to the point that the secondary particles would act as rigid inclusions, and not as reinforcements [38]. Moreover, it is worth noting that the high cooling rates which are often observed in AM are responsible for a sensible refinement of in-situ grown TiB and other reinforcements as compared to conventional manufacturing techniques, and this avoids the formation of large intermetallics that are known to act as stress-concentration sites [21].

The efficacy of B in modifying the microstructural features of Ti and its alloys, even if added in trace amounts, is paramount in light of the stringent specifications prescribed by ASTM F2924-14(2021) [39] on the acceptable composition of Ti-6Al-4V parts produced by PBF. Whilst specific tolerances are given for Al, V, Fe, O, C, N, H

and Y, all other elements have a maximum allowance of 0.1 wt.% if taken individually, up to a combined limit of 0.4 wt.% in total. This means that microstructural manipulation ‘according to standard’ can only be pursued through element additions in ‘trace levels’ [14]. However, it should be mentioned that the identification of the ‘optimal’ or ‘required’ B amount in Ti and Ti-alloy parts produced by AM is still an open challenge. For example, Zhang et al. [13] observed that adding trace amount of B (≤ 1.0 wt.%) was sufficient for triggering the CTE transition of prior- β grains, for eliminating disadvantageous α forms such as grain boundary α , and for promoting the formation of refined α laths with a reduced aspect ratio and a weakened texture. On the other hand, Zhang et al. [13] also noticed a progressive loss of ductility on increasing the filler loading. Ultimately, B addition by 0.05 wt.% was recommended for achieving balanced tensile properties. Conversely, He et al. [40] applied a PBF-LB powder-free method (which means that single tracks were laser-scanned in arc-melted buttons) to investigate the combination of Ti-6Al-4V and B over a wide compositional range up to 10 wt.% of B. For each composition, 14 different sets of laser power and scan speed were tested. Based on the analysis of the 70 single scans thus generated, He et al. [40] concluded that promising B contents for Ti-6Al-4V composite parts manufactured by PBF-LB lie between 2 and 5 wt.% of B, because the corresponding composite systems in this range presented a large processing window, produced a stable melt pool whose size corresponded closely to that of unmodified Ti-6Al-4V, and entailed a promising microstructure consisting of a TiB network with submicron spacing.

While research is growing in the literature, a review that summarises the main findings regarding the role of B in the microstructural manipulation of additively manufactured Ti-based parts is still missing. In order to bridge this gap, the present review provides a critical discussion of the microstructural evolution occurring in B-modified Ti and Ti alloys while printing. Detail is also provided regarding grain refinement, columnar-to-equiaxed transition, and densification, as the main structural aspects that will govern the part’s performance in service. The microstructure-performance relationship is elucidated with an emphasis on hardness, compressive and tensile properties, as these are the parameters most frequently reported in the literature. In doing so, open challenges are clearly outlined. Gaining a deeper understanding of B-induced microstructural changes appears to be critical for the wider adoption of additively manufactured Ti-based parts in industry, taking into consideration the importance of improving their mechanical behaviour in performance-critical applications.

2. Microstructural evolution

2.1. B-driven solidification pathways in AM

B can be introduced as elemental B, in which case B can be either pre-alloyed within the feedstock powder, or simply pre-mixed with it. In the latter case, great attention is usually paid to achieving a uniform distribution, for example pre-mixing by ball milling, without affecting the original morphology and size distribution of the Ti or Ti alloy particles [41,42], as well as the ‘flowability’ of the feedstock. Some AM technologies may require specific procedures, though, such as painting the substrate with a B-based painting in WAAM [6].

While B is completely soluble in the liquid phase of Ti [28], the solidification pathway upon cooling depends on the B concentration in the liquid. The Ti-B binary phase diagram is shown in Figure 3. In principle, the eutectic composition in the Ti-B binary system corresponds to a composition of Ti-1.6B (wt.%) at a temperature of 1540 °C [21]. Sometimes, compositions below the eutectic limit are considered as B-modified Ti or Ti alloy, because their microstructure-processing-property relationships are similar to those of the base metal/alloy without B. However, it should be emphasised that hypoeutectic compositions may still contain eutectic TiB precipitates, and this makes them discontinuously reinforced TMCs [43]. When it comes to AM, the hypereutectic vs. hypoeutectic classification based on the equilibrium phase diagram does not hold true anymore. The melt pool in AM is a highly dynamic environment. Along with the energy density, the efficiency of the Marangoni convection flow is largely responsible for redistributing B uniformly within the melt pool [37,44]. The diffusion of B may also be affected and prematurely interrupted by the short time frame available for solidification in the melt pool [30,44]. On the other hand, the high cooling rates commonly observed in most AM methods may cause the entrapment of B in a super-saturated matrix and cause a shift of the eutectic point [45].

Ultimately, regardless of the nominal composition of the starting feedstock powders, the content of B may fluctuate and the composition within the melt pool may locally become hypereutectic [24,46].

A schematic of the solidification pathways for hyper- and hypo-eutectic compositions is shown in Figure 4.

2.1.1. Hypereutectic compositions

For hypereutectic compositions, the solidification pathway (dashed line in Figure 3) can be modelled as: Liquid \rightarrow Liquid + Primary (proeutectic) TiB \rightarrow Primary TiB + Eutectic TiB + β -Ti \rightarrow Primary TiB + Eutectic TiB +

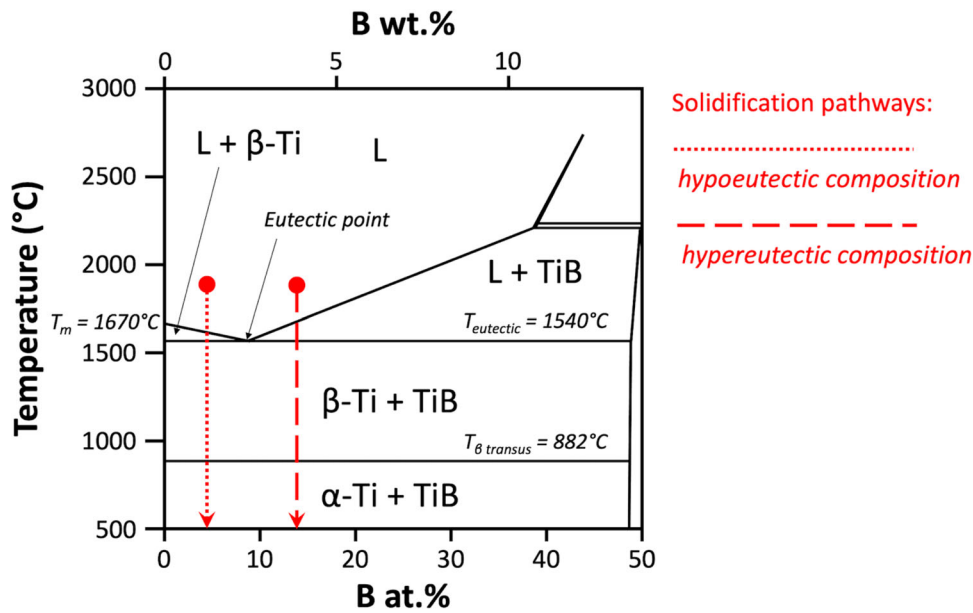


Figure 3. Ti-B binary phase diagram, shown up to 50 at.% of B, corresponding to the composition of TiB, as the commonest range explored in AM.

α -Ti. The microstructural evolution is schematically illustrated in Figure 4a. For Ti alloys, both the α and/or β phase can be present at room temperature depending on the specific alloy composition. Although deviations from equilibrium may occur because of fast cooling in AM [44], the final microstructure of hypereutectic parts is thus expected to include relatively large prismatic primary (pro-eutectic) TiB particles in addition to the prevailing needle-like eutectic TiB nanowires/whiskers dispersed in an α and/or β matrix [21,24,47,48]. Coarse primary TiB precipitates may retain a nanoscale Ti core, as already noticed by Banerjee et al. [47] and by Kooi et al. [49]. Maybe because of this metal core, primary TiB precipitates are sometimes described as ‘hollow’ (examples in the contributions by Lenivtseva et al. [50] and by Xue et al. [51]).

In principle, TiB₂ may also form from the reaction between Ti and B in the melt pool, especially after a local enrichment in B such as, for example, around the dissolving B particles. However, due to the abundance of Ti in the reaction zone, TiB₂ is likely to react with the surrounding Ti matrix, thus giving additional TiB [19,30,52]. Additionally, while the formation of TiB₂ would be energetically favoured, the kinetics may be very slow. According to diffusion bonding experiments between Ti-6Al-4V foils and C/TiB_x-coated SiC fibres in a temperature range between 870 and 970°C, Fan et al. [53] estimated that the diffusion coefficient for B in TiB along the needle direction is about 45 times higher than that in TiB₂, although the diffusion activation energy is the same in both TiB and TiB₂ (187-190 kJ/mol).

According to the solidification model proposed by Hu et al. [24,46], the liquid Ti solidifies as β -Ti upon cooling through heterogeneous nucleation at the surfaces of primary TiB crystals and through homogeneous nucleation from the liquid. Since the atomic radius of B (1.17 Å) is relatively large, the diffusivity and solubility of B in solid Ti are very low [31,33]. B is thus expelled from the β -Ti nuclei to the surrounding liquid, where B reacts with the liquid Ti matrix and precipitates in the form of eutectic TiB nanowhiskers [28]. Eutectic TiB nanowhiskers preferentially aggregate at the boundaries of the newly crystallised β -Ti grains [24,54]. Primary (hypereutectic) TiB precipitates are also forced to the β grain boundaries, where they may act as nucleation sites for the formation of eutectic TiB [30].

It has been argued that, due to the rapid solidification of the melt in AM, there might be not enough time for the eutectic reaction between Ti and B to reach completion, in which case the solidified β -Ti phase would retain a supersaturation of B [55]. Nonetheless, it should be noted that not all AM techniques are the same, and the cooling rates may actually be quite different. For example, cooling rates in PBF-EB have been reported to be lower by an order of magnitude to those in PBF-LB [56]. As shown in the solidification/processing map published by Birmingham et al. [57], cooling rates may exceed 10⁵ °C/s in PBF-LB, range indicatively between 10² and 10⁴ °C/s for DED-LB, and lay around 10² °C/s for wire-fed DED, i.e. WAAM. The cooling rates in WAAM can be even lower depending on the processing conditions (for example, while analysing the effect of substrate pre-heating on the bead

Effect of cooling

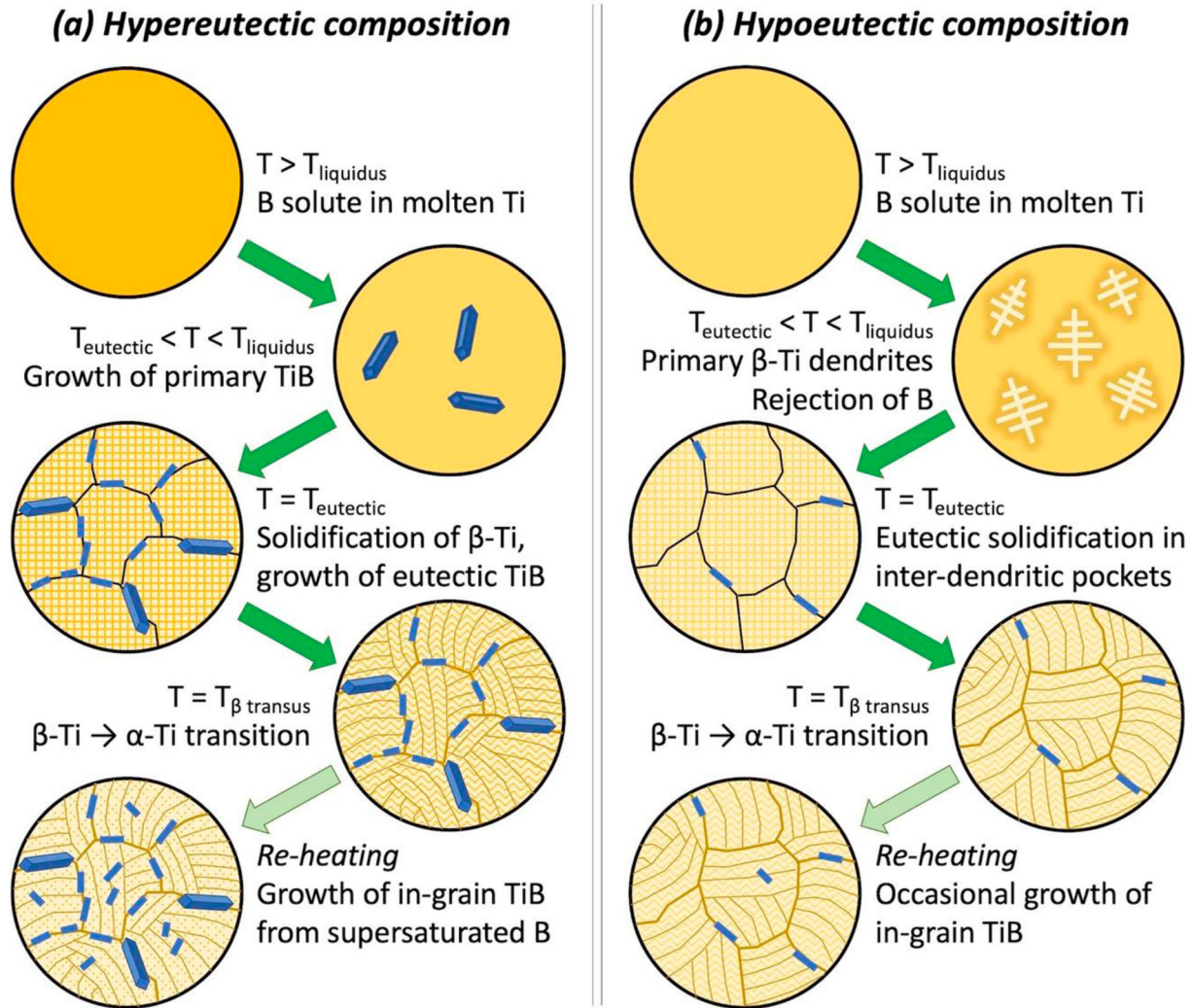


Figure 4. Microstructural evolution occurring upon cooling for (a) hypereutectic and (b) hypoeutectic Ti-B compositions.

geometry of Inconel 625 processed by WAAM, Gudur et al. [58] recorded cooling rates as low as 14°C/s thus approaching the cooling rates observed in casting [59]. Even in case the cooling rate is sufficient for prematurely interrupting the eutectic reaction, the decomposition of the matrix into eutectic TiB + β -Ti is favoured by local reheating as additional layers are being deposited [21]. In this case, fine (nanoscale) TiB particles would precipitate inside the Ti grains by cyclic heating and cooling [60,61]. These ‘delayed’ TiB nanowhiskers grow through solid state reactions within the supersaturated α matrix, and this is likely to facilitate the establishment of orientation relationships, thus leading to strong TiB-Ti interfaces, as already observed by Banerjee et al. [60].

Although additional TiB nanowhiskers may form within the grains during re-heating, Hu et al. [24,46,62] noticed that the preferential arrangement of primary

and eutectic TiB at the grain boundaries of the prior β -Ti grains survives to room temperature through the $\beta \rightarrow \alpha$ transformation. Hu et al. [24,46,62] hypothesised that the growth of this nearly continuous interconnected network (‘quasi-continuous network’, QCN) of reinforcements can be beneficial, since the TiB-rich regions at the grain boundaries are responsible for strengthening the composite, while the TiB-poor regions within the grains retain the ductility of the Ti matrix. Analogous conclusions were drawn by Singh et al. [63] with regard to Ti-6Al-7Nb parts processed by PBF-LB, whose microstructure was characterised by a QCN of TiB precipitates due to the addition of 3 wt.% of TiB_2 (corresponding to 0.90 wt.% of B).

As the temperature decreases further, TiB is a potent nucleant for heterogeneous nucleation of the α phase. As observed by Yang et al. [64], although this point is

often overlooked in the literature, a peritectoid reaction occurs at nearly 884–886°C, whereby β -Ti would react with TiB upon cooling to form α -Ti (i.e. β -Ti + TiB \rightarrow α -Ti) [65,66]. This reaction is often neglected as it overlaps the β transus, which occurs at 882°C for pure Ti, although the addition of B is known to increase the β transus of both cp-Ti and Ti-6Al-4V in casting and powder metallurgy processing [67,68]. However, the peritectoid reaction justifies the strong nucleating effect of TiB for the α phase, which should nucleate directly on TiB if their lattice parameters match well, and certain crystallographic orientation relationships exist [64].

Yang et al. [64] estimated that, in principle, the lattice mismatch between the 'a' axis of the α -Ti matrix (hexagonal structure) and the 'b' axis of TiB (orthorhombic structure) is 3.6%, and the lattice mismatch between the respective 'c' axes is 2.8%. However, it was recognised that the exact orientation relationships between TiB and α -Ti may change according to the chemistry and the processing conditions [64]. Moreover, the establishment of orientation relationships between TiB and α -Ti grains is quite complicated because it is mediated by the β transus. Although deviations may occur in AM due to repeated heating and cooling cycles [63], the $\beta \rightarrow \alpha$ transition is predicted to occur according to the Burgers orientation relationships between the α/β lattices, and this gives 6 orientation variants (12 including directions) for the nucleation of the α phase [8]. Using spark-plasma sintered TMCs as an experimental model, Ozerov et al. [69] noticed that, if an orientation relationship exists between TiB and prior- β grains, the $\beta \rightarrow \alpha$ transition will thus translate into 6 orientation variants between TiB and the α phase. Among them, the most likely variants are those that minimise the structural mismatch and hence the structural energy of the system. Stacking faults may also play an important role in decreasing the lattice mismatch between TiB and the surrounding matrix [47,70,71]. This is coherent with the results presented by Otte et al. [30] for as-printed PBF-LB parts. Numerous stacking fault defects could be observed at the interface between TiB and α -Ti matrix, and this led to a strong structural continuity at the interface. In this regard, it is worth noting that TiB may exist in the Ti matrix in two polymorphs, namely the B27 orthorhombic structure (stable) and, although less common, the B_f orthorhombic structure (metastable) [49]. These structures are closely related, given that the B27 structure corresponds to the B_f structure by introducing stacking faults on the B27 (2 0 0) planes [60]. While Genç et al. [72] described the formation of a complex intermixed structure with a prevalent B27 matrix interrupted by thin B_f regions extending laterally across the entire boride precipitate, according to the results

presented by Kooi et al. [49] the B27 form is wrapped by a thin layer of the B_f form that reduces the interface energy with the surrounding Ti matrix. Generally, the greatest part of the literature elaborates on the orientation relationships existing between TiB and α -Ti because, as mentioned above, α -Ti is the stable polymorph of Ti at room temperature in cp-Ti (no β stabilisers). Moreover, the morphology of α grains deeply affects the ductility of $\alpha + \beta$ alloys (e.g. Ti-6Al-4V) and nearly β alloys [64]. However, Feng et al. [73] demonstrated that (1 0 0) TiB planes are well bonded through semi-coherent interfaces with both the α -Ti and the β -Ti matrix, which is consistent with previous experimental findings by Li et al. [74].

However, contradictory results can be found in the literature regarding the orientation relationship between TiB and the surrounding matrix in AM parts. For example, according to Banerjee et al. [21], a striking difference could be observed between primary and eutectic TiB precipitates in cp-Ti parts modified with 2 wt.% of B produced by DED-LB. While a coherent orientation relationship was generally observed between the eutectic TiB phase and the adjacent α phase, primary TiB precipitates did not exhibit any specific orientation relationships with the α matrix. This was justified by the different genesis of primary TiB, which nucleates and grows as a result of primary solidification in the liquid phase, as opposed to eutectic TiB, which forms through eutectic solidification in close continuity with the Ti matrix [21]. Nonetheless, as seen before, TiB should be a nucleant for the α phase at the peritectoid, and this should produce definite orientation relationships. On the other hand, after re-indexing, the electron backscattered diffraction (EBSD) scans published by Zhang et al. [13] demonstrated that most of the TiB whiskers identified in Ti-6Al-4V parts with either 0.5 or 1 wt.% of B (processed by DED-LB) had no specific orientation relationships with their surrounding α matrix. This suggests that the establishment of orientation relationships between TiB whiskers and surrounding α matrix is not automatic, even if the composition is hypoeutectic and primary TiB should thus be absent. In this regard, future investigation would be required to understand why orientation relationships may be inconsistent in additively manufactured TMCs, keeping in mind that having structural continuity at the interface facilitates the matrix-to-reinforcement load transfer in TMCs. Ascertaining the existence of orientation relationships may be particularly challenging in Ti-6Al-4V and other $\alpha + \beta$ alloys, because the large volume fraction of α phase may make it difficult to precisely identify where each a domain nucleated from [75].

2.1.2. Hypoeutectic compositions

When Ti is modified with small amounts of B (in the order of ≈ 0.5 wt.% or lower according to the observations of Bermingham et al. [14], but the actual Ti-B eutectic point may depend on the specific system under exam, given that Attar et al. [41] observed a hypoeutectic solidification process for cp-Ti parts containing 5 wt.% of TiB_2 , which would correspond to 1.5 wt.% of B), the solidification pathway is different, because the composition of the melt pool is expected to remain hypoeutectic in spite of potential local fluctuations. According to the binary phase diagram (dotted line in Figure 3), for hypoeutectic compositions primary TiB does not form anymore, as β -Ti crystallises first [21].

As summarised by Losert et al. [76], the solidification morphology of a given alloy largely depends on the growth speed, meaning that, when solidification occurs rapidly, the originally planar solid-melt front becomes unstable and changes to a pattern of cells, which are initially shallow, and then increasingly deep. Ultimately, the cells transform to dendrites with a branched structure. The main reason for this instability of the solidification front has been identified as constitutional supercooling. Since the solute is typically more soluble in the melt than in the solid, solute rejection occurs ahead of the solidification front. Due to the freezing-point depression, the compositional gradient produces a gradient in crystallisation temperature (i.e. the local crystallisation temperature increases with distance from the solidification front, since the solute concentration is progressively lower). If the crystallisation temperature gradient exceeds the actual temperature gradient at the solid-melt interface, the solidification front becomes unstable.

Whether a molten alloy will solidify in a planar, cellular, or dendritic microstructure depends on its composition as well as on the solidification conditions. As for the composition, the experimental work conducted by Bermingham et al. [59] suggests that solidification of both cp-Ti and Ti-6Al-4V castings (initial cooling rates exceeding 150°C/s over the first 1–2 s, then decreasing to approximately 30°C/s during the $\beta \rightarrow \alpha$ transition) happens through dendritic growth. The addition of B further promotes dendritic solidification due to the partitioning coefficient of B in Ti approaching 0 [59,67]. In terms of processing conditions, it is generally recognised that metal AM proceeds through localised solidification processes occurring within the melt pool under steep thermal gradients and high cooling rates, which is expected to promote dendritic-columnar structures (which is illustrated in the solidification/processing

map published by Bermingham et al. [57]). As mentioned above, though, the cooling rates can be different for different AM technologies, sometimes by orders of magnitude, such that in WAAM the solidification mechanism of Ti-6Al-4V can be controlled to become mixed equiaxed \pm columnar, rather than dendritic [77].

In light of this, it may be reasoned that the Ti in hypoeutectic Ti-B systems must have a strong propensity to nucleate and grow via a dendritic mechanism in most AM technologies (as explained earlier, hypereutectic systems follow different solidification pathways owing to the primary crystallisation of TiB [78]). However, it should be mentioned that, especially in technologies like PBF-LB that implicitly have extremely high cooling rates, solidification may occur under highly dynamic non-equilibrium conditions (to the point that compositional undercooling may be suppressed), thus leading to microstructures that differ from those commonly observed in casting [79]. Generally speaking, the solidification mechanisms for a given composition will be strongly affected by the cooling rate, which depends on the processing parameter [80]. Additionally, the presence of ceramic particles may perturb the convection flow within the melt pool and reverse it, which may pull out the dendrites growing upwards from the previously deposited layer and drag them back to the core of the melt pool, thus interfering with the formation of an ordered dendritic pattern [77]. The microstructure of additively manufacture parts may ultimately change as a result of re-heating, as already seen for hypereutectic Ti-B compositions.

Taking into account the solidification of primary Ti in a dendritic morphology, the microstructural evolution for hypoeutectic systems is exemplified in Figure 4b. In this regard, B is known to decrease the equilibrium liquidus temperature of Ti. For example, a drop in the solidification temperature of nearly $15\text{--}20^\circ\text{C}$ (from around 1679°C to around $1660\text{--}1662^\circ\text{C}$) was detected in a Ti-6Al-4V matrix modified with 0.05 wt.% of B and processed by WAAM [14]. As the temperature decreases, B remains in the molten Ti, where it is progressively rejected between the growing β -Ti dendrites (or columnar grains, depending on the specific solidification mechanism). B progressively accumulates, and then precipitates as eutectic TiB within the pockets of liquid remaining between impinging β -Ti dendrites [54]. As pointed out by Bermingham et al. [14], in metal AM the delayed growth of TiB particles in hypoeutectic systems occurs between previously solidified columnar grains and/or within interdendritic pockets, thus leading to a preferential orientation of the eutectic TiB

whiskers along the growth direction. The formation of strongly oriented TiB needles has actually been observed for Ti-6Al-4V parts fabricated by WAAM with trace LaB_6 and with trace (elemental) B [14]. However, it should be mentioned that the processing conditions and typical cooling rates experienced in WAAM are sensibly different from those observed in PBF-LB and DED-LB, and this may result in different microstructures, where lower cooling rates often favour coarser microstructural features [55].

2.1.3. Solidification pathways: A summary

The final microstructure of B-modified parts largely depends on the interaction between feedstock composition and processing parameters. In principle, a key design parameter is the eutectic composition, corresponding to about 1.6 wt.% of B. However, the complicated dynamics within the melt pool may affect the distribution of B, such that the local concentration may become hyper- or hypo-eutectic regardless of the nominal composition. Owing to the short solidification time generally available in AM, incomplete B dissolution has sometimes been reported in the literature, for example in the investigation conducted by Hu et al. [24].

Examples of the typical microstructures resulting from the addition of B to Ti and Ti alloys in AM are displayed in Figure 5 [40]. Additional detail regarding experimental research in B-modified Ti and alloys is listed in Table 1 [6,11,13,21,24,42,46,47,51,55,60,62,72,81,82]. The last column in Table 1 provides information regarding the mechanical properties of B-modified Ti-based parts, which are discussed further in Section 8.

2.2. Effect of B on post-printing heat treatment

Finally, it is worth mentioning that adding B offers additional advantages whenever the Ti-based component is due to receive a post-printing heat treatment or is expected to work in a high-temperature environment. Owing to their thermal and chemical stability, TiB and other ceramic particles (if present) are predicted to remain unaffected when exposed to elevated temperatures [47], although Otte et al. [30] documented a slight coarsening of TiB needles with a disproportional increase in length relative to the diameter when LB-PBF parts made of cp-Ti with 2.5 vol.% of BN were heat-treated in a vacuum furnace at 900°C for 6 h (heating and cooling rates of 2°C/min). Provided that TiB whiskers remain nanosized, the increased aspect ratio without lateral coarsening is expected to ameliorate the overall mechanical performance of the composite owing to the increased interfacial contact area

between the matrix and the reinforcement [30]. Moreover, TiB and other ceramic particles do not melt nor dissolve in the surrounding metal matrix when heat-treated, and their permanence at the grain boundaries avoids grain growth by Zener pinning [6,19,30]. The impact of grain size on the mechanical properties is discussed further in Section 8. Besides the mechanical properties, TiB and other ceramic particles enhance the oxidation resistance of Ti. As summarised by Avila and Bandyopadhyay [19], at room temperature Ti has a protective oxide layer (titanium dioxide, TiO_2), about 4–5 nm thick. If Ti is heated up to 600°C, the oxidation kinetics are parabolic, which means that the passivation layer hinders the diffusion of oxygen into the bulk material, such that the diffusion of oxygen becomes the rate controlling step. However, if the temperature exceeds 600°C, cracks and pores undermine the continuity of the passivation layer, and the oxidation kinetics change from parabolic to linear with continuous and unrestricted uptake of oxygen. Avila and Bandyopadhyay [19] demonstrated that the addition of 6 wt.% of BN to cp-Ti parts produced by LB-DED was sufficient to reduce the oxidation rate by a factor of 4 and to cut down the change in mass associated with oxidation by 35.3% after 50 h at 1000°C under controlled air flow (40 mL/min). The increased oxidation resistance was attributed to the BN-induced microstructural modification of the DED-LB printed parts, leading to a refined microstructure, and to the in-situ formation of hard and thermally stable TiB and TiN particles. While the oxidation resistance improved as the BN concentration was increased from 3 to 6 wt.%, Avila and Bandyopadhyay [19] pointed out that the presence of unreacted BN particles due to excessive filler loading may be counterproductive and ultimately reduce the thermal stability in air because of the intrinsically poor oxidation resistance of this compound. Interestingly, the presence of unreacted BN is less critical if the heat treatment is conducted under vacuum. In the absence of oxygen, residual BN can react with Ti, which triggers the growth of additional TiB after thermal treatment [30].

3. Non-elemental B sources

Various non-elemental sources of B have been explored in the AM of Ti and Ti-alloy parts, including CrB_2 [83], yet the most popular are currently TiB_2 , BN, LaB_6 and B_4C , as further discussed in the following sections.

3.1. Titanium diboride (TiB_2)

TiB_2 is a convenient source of B, which does not bring in any additional elements other than B (as the

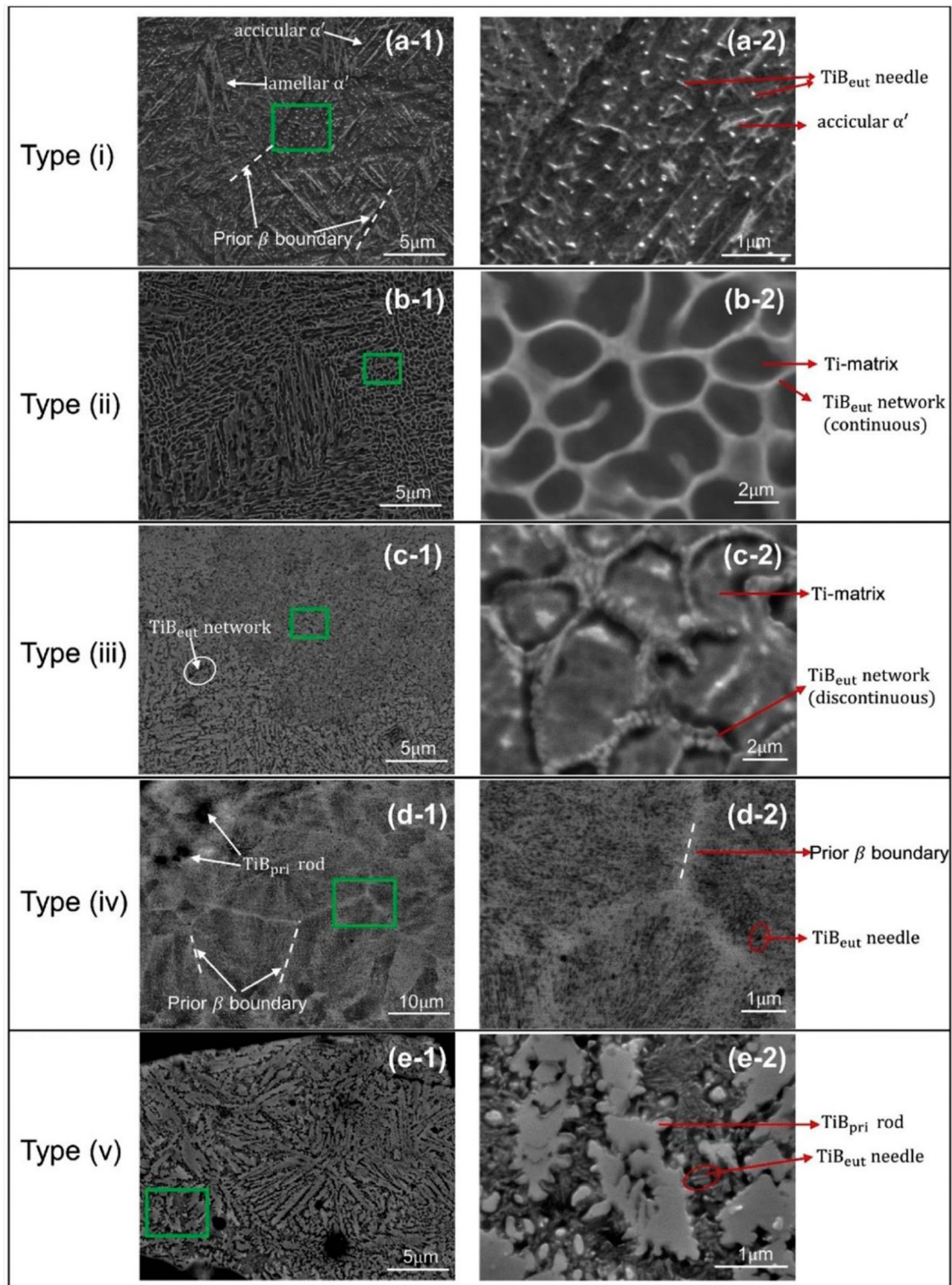


Figure 5. Scanning electron microscopy (SEM) micrographs showing microstructures ('types') commonly observed in Ti-6Al-4V additively manufactured parts modified with B. Type (i), showing uniformly-distributed eutectic TiB whiskers ((a-1), (a-2)); Type (ii), showing continuous TiB network ((b-1), (b-2)); Type (iii), showing discontinuous TiB network ((c-1), (c-2)); Type (iv), showing both nano-scale eutectic TiB needles and primary TiB rods ((d-1), (d-2)); and Type (v), showing dendritic primary TiB rods and nano-scale eutectic TiB needles ((e-1), (e-2)). Images on the right, labelled as '2', are high-magnification images of the corresponding green boxes in the low-magnification images on the left, labelled as '1'. Reproduced from He et al. [40] under the Attribution-Non-Commercial-NoDerivatives 4.0 International (CC BY-NC-ND 4.0) license, <https://creativecommons.org/licenses/by-nc-nd/4.0/>.

Table 1. Experimental contributions discussing the addition of B to Ti and Ti alloy parts produced by AM.

| Paper | AM parameters | Matrix | Filler | Loading | Microstructure ^(a) | Properties ^(a) |
|---------------------------|---|--------------------|------------------------------------|---|--|---|
| DED-LB: | | | | | | |
| Banerjee et al. [21] | Constant | cp-Ti | B particles | 1 wt.% 2 wt.% | Bimodal distribution of primary and eutectic TiB Refined TiB size in AM vs. arc melted composites (primary TiB reduced from 20–100 µm to 0.5-3.0 µm) | Berkovich nanohardness of 130 and modulus of 4.6 GPa at 2 wt.% B |
| Banerjee et al. [47] | Constant (+ heat treatment) | Ti-6Al-4V | B particles | 2 wt.% | Primary and eutectic TiB No coarsening of TiB precipitates after heat treatment Refined α/β microstructure Equiaxed α phase, instead of lath-type | – |
| Banerjee et al. [60] | Constant | cp-Ti Ti-6Al-4V | B particles | – | Bimodal distribution of (nano/micro) TiB TiB with B27 and B _f orthorhombic structure TiB at grain boundaries and within grains | – |
| Genç et al. [72] | Constant | cp-Ti | B particles | 2 wt.% | Stacking faults in B27 form of TiB resulting in B _f form Orientation relationship between TiB and Ti | – |
| Hu et al. [24] | Assessment of laser power | cp-Ti | B particles (size: 2 µm) | 1.6 wt.% | Quasi-continuous network of primary and eutectic TiB for high laser power Balling defects due to poor wettability of TiB | Increasing hardness with increasing laser power Increased hardness by 29.3% Decreased wear rate by one order of magnitude (87.3% lower) |
| Hu et al. [42] | Assessment of laser power Assessment of z-axis increment | cp-Ti | B particles (size: 2 µm) | 1.6 wt.% | Flower-like morphologies with TiB emanating from central pore Increasing density with increasing power (energy density) for both Ti and TMC Decreasing density with increasing z-axis increment for both Ti and TMC | Increasing hardness with increasing laser power Almost unchanged hardness with increasing z-axis increment Increased hardness for TMC Increased ultimate strength under compression Reduced ductility (deformation at break) under compression |
| Hu et al. [46] | Assessment of laser power | cpTi | B particles (size: 2 µm) | 1.6 wt.% | Quasi-continuous network of primary and eutectic TiB for high laser power | Increased yield strength under compression at any laser power level Increased ultimate strength under compression at any laser power level Decreased ductility under compression at any laser power level Decreased toughness under compression at any laser power level |
| Hu et al. [62] | Assessment of laser power | cp-Ti | B particles (size: 2 µm) | 1.6 wt.% | Quasi-continuous network of primary and eutectic TiB for high laser power | Increased hardness from 304 HV to 393 HV Increased compressive strength from 761 MPa to 1051 MPa Decreased ductility/deformation at break from 64.9% to 26.2% |
| Huo et al. [81] | Preliminary laser power optimisation (+ annealing at 950°C for 4 h) | Ti-45Al-8Nb | B, pre-alloyed | 0.5 at.% | Refined lamellar colony grains, from 75 to 45 µm Decreased non-uniformity factor, from 2.65 to 1.99 Weakened phase transformation texture, from 58 to 20 TiB with orthogonal B27 structure | Increased ultimate tensile strength by 8% Increased elongation at break by 51% |
| Rahman Rashid et al. [55] | Constant | Ti-6Al-4V | Amorphous B particles (size: 1 µm) | 0.05 wt.% | Discontinuous β-Ti grain boundaries Fine α laths instead of α' martensite needles Very fine TiB | Increased hardness from 390-450 HV to 510–600 HV |
| Xue et al. [51] | Constant | Ti-6Al-4V | Amorphous B particles (size: 1 µm) | 0.1 wt.% (real: 0.08) 0.2 wt.% (real: 0.17) 0.3 wt.% (real: 0.25) | Refined prior β-Ti grains Prior β-Ti grains epitaxial for B < 0.08 wt.%, and alternating columnar and equiaxed dendrites for B > 0.17 wt.% Reduced length of grain boundary α Reduced size of colony α For low B content, TiB arranged between β dendrites and preferentially oriented | Increased ultimate tensile strength Increased yield strength Decreased ductility (deformation at break) Reduced anisotropy |

(Continued)

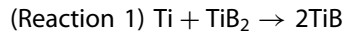
Table 1. Continued.

| Paper | AM parameters | Matrix | Filler | Loading | Microstructure ^(a) | Properties ^(a) |
|---|---|-----------|--------------------------|--|--|---|
| Zhang et al. [11] | Constant (+ annealing at 700°C for 2 h) | Ti-6Al-4V | B, pre-alloyed | 0.05 wt.% | Mixed equiaxed/columnar grain structure More homogeneous and refined prior-β grains, with reduced width from 314 μm to 76 μm Reduced prior-β grain aspect ratio from 3.8 to 2.7 More equiaxed and refined α grains, with reduced width from 1.05 μm to 0.81 μm Reduced α grain aspect ratio from 14.95 to 8.27 Traces of randomly dispersed TiB | Increased tensile yield strength from 862 MPa to 904 MPa Increased ultimate tensile strength from 933 MPa to 982 MPa Retained ductility with elongation at break almost unchanged from 10.2% to 10.0% Tensile fracture surface with large and flat region of stable crack propagation High-cycle fatigue life increased by an order of magnitude at 550 MPa (even more significant difference at 450 MPa) Smooth fatigue crack propagation profile Faster fatigue crack propagation rates by nearly one order of magnitude |
| Zhang et al. [13] | Same for all (+ annealing at 700°C for 2 h) | Ti-6Al-4V | B, pre-alloyed | 0.05 wt.% 0.5 wt.% 1.0 wt.% | Refined β grains, from >400 μm to <90 μm Reduced texture index of α phase, from 36.4 to 1.7 Reduced α lath thickness Suppression of grain boundary α, from 1.23 to 0.59 μm TiB growth; TiB clusters at 0.5 and 1 wt.% B | Increased tensile strength Reduced anisotropy under tension Decreased ductility under tension Brittle failure above 0.05 wt.% of B |
| PBF-EB: Mahbooba et al. [82] | Constant | Ti-6Al-4V | B, pre-alloyed | 0.25 wt.% 0.5 wt.% 1.0 wt.% | Reduced prior-β grain thickness Reduced α aspect ratio Reduced α lath area | Increased microhardness by 26% max Increased elastic modulus by 9% max Reduced ductility |
| WAAM: Bermingham et al. [6] | Constant (+ annealing at 480°C for 2 h) | Ti-6Al-4V | B, paint on substrate | 0.05 wt.% 0.15 wt.% (real: 0.13) | Minor fraction of TiB Reduced prior-β grain thickness from 1823 to 339 μm Reduced α aspect ratio (by a factor >4) Suppressed colony α Suppressed grain boundary α | No effect on compressive properties in as-deposited parts Increased compressive ductility by 40% after heat treatment Mitigated large-scale twinning Increased nanohardness from 4.77 GPa to 27.00 GPa |

^aIf not otherwise stated, for each contribution the benchmark is the corresponding B-free metal matrix.

microstructure modifier) and Ti itself (as the main component of the matrix). TiB_2 , like most ceramic fillers, has a higher laser absorption coefficient than Ti, which favours the absorption of energy (heat) in laser-based AM processes [70].

In spite of being the most stable Ti boride in the Ti-B system, TiB_2 melts/dissolves upon printing and reacts with the Ti matrix to produce TiB according to [44].



Two possible mechanisms have been proposed for the formation of TiB starting from TiB_2 . TiB can be generated either by diffusional removal of B from TiB_2 into the Ti matrix, or by melting of TiB_2 and subsequent formation of TiB during solidification. In this regard, Attar et al. [41] commented that both options are possible, but extensive diffusion removal of B would take too long if compared to the short solidification time available in PBF-LB, which makes the melting/solidification route more likely. In principle, in-situ TiB_2 might also form through the melting/solidification route. As a matter of fact, given the lower enthalpy of formation, TiB_2 ($-53.0 \text{ kcal/mol} \cong -221.8 \text{ kJ/mol}$) should be thermodynamically favoured over TiB ($-28.0 \text{ kcal/mol} \cong -117.2 \text{ kJ/mol}$). Nonetheless, TiB is known to form instead of TiB_2 as soon as the concentration of B in the reaction zone falls below 18-18.5% [19,52]. Finally, it is worth noting that Reaction 1 is strongly exothermic, with the reaction enthalpy being -45 kJ/mol at 2300°C . As a term of comparison, the heat of fusion of neat Ti is just 15.45 kJ/mol , which means that 3 mol of Ti can be melted due to the reaction between 1 mol of Ti and 1 mol of TiB_2 [44].

Occasionally, depending on the printing parameters and the filler loading, some TiB_2 has been reported to remain unreacted into the printed part, thus resulting in a (hybrid) ex-situ TiB_2 /in-situ TiB TMC (for example, in the contributions by Chen et al. [35] and by Galvan et al. [44]). However, in-situ grown reinforcements offer key advantages over ex-situ ones, since the filler distribution in the final part is more homogeneous, and the size of the reinforcing phase can be controlled through the processing conditions to remain smaller than ex-situ counterparts [24]. Moreover, as previously mentioned, the clean interface between in-situ reinforcement and surrounding matrix is key to enabling an efficient load transfer [84]. Another advantage of in-situ TMCs is that TiB is in thermo-dynamic equilibrium with the matrix, and hence thermally stable and resistant to coarsening when subject to heat treatment [47]. Accordingly, as discussed by Wang et al. [85], the printing conditions

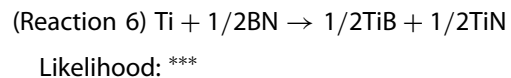
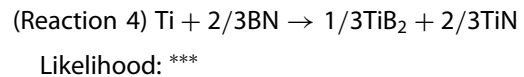
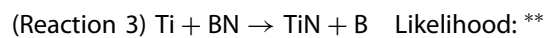
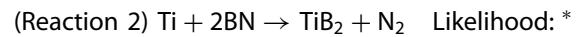
should be adjusted to induce the complete dissolution of primary borides, thus making the whole amount of B introduced into the system available for microstructural refinement and formation of secondary TiB.

Examples of experimental work conducted in TiB_2 -modified systems are provided in Table 2 [2,23,35,41,44,63,70,85–90]. The mechanical behaviour of TiB_2 systems, briefly summarised in the last column of Table 2, is analysed in Section 8 below.

3.2. Boron nitride (BN)

Boron nitride (BN) is a common precursor for B. By itself, BN is an insulating ceramic material with good thermal conductivity and high melting point (2973°C). However, unless nanostructured [48], BN has limited mechanical strength and low hardness, and suffers from poor oxidation resistance [91]. Although BN also exists in the cubic form [92], hexagonal BN is the commonest form employed for the AM of TMCs.

At equilibrium, numerous reactions are possible in the Ti-BN system depending on the system's stoichiometry [19,93]:



where the 'likelihood' of each reaction has been rated according to the reaction enthalpies tabulated by Borisova et al. [93]. Based on thermodynamic considerations, the most probable scenario occurring in the temperature range between 500 and 2000 K is the formation of a mixture of Ti borides and nitrides according to Reactions 4 and 6 [19,93]. As mentioned above, TiB_2 should be thermodynamically favoured over TiB and therefore TiB_2 would be expected to form in the initial reaction occurring between B and Ti around BN particles. Nonetheless, as previously explained, TiB_2 is likely to be consumed to TiB by Reaction 1 [19,52].

While reactions 2–6 refer to equilibrium conditions, in metal AM the high energy density delivered by the incident beam (or other energy source) and the high cooling rates favour out-of-equilibrium reactions [94]. Metastable phases and polymorphs can be locked in, and

Table 2. Experimental contributions discussing the addition of TiB₂ to Ti and Ti alloy parts produced by AM.

| Paper | AM parameters | Matrix | Filler | Loading | Microstructure (°) | Properties (°) |
|--------------------|---|-----------------|--|--|--|---|
| DED-LB: | | | | | | |
| Galvan et al. [44] | Identification of processing window | cp-Ti | TiB ₂ particles (5-25 µm) | Ti:TiB ₂ = 2:1 wt./wt. Ti:TiB ₂ = 1:2 wt./wt. | Less unreacted TiB ₂ at lower scan speed Enhanced TiB ₂ dissolution at higher power Different titanium borides at different laser power and filler loading Strong interface between TiB (both eutectic and primary) and Ti matrix | TiB hardness of 30.7 GPa TiB Young's modulus (from indentation) of 519 GPa Hardness of eutectic layer of 7.5 GPa Increased 'relative wear resistance', especially for eutectic microstructure |
| Wang et al. [85] | Assessment of laser power (+ annealing or HIP for tensile testing) | Ti-6Al-4V | TiB ₂ particles (5-50 µm) | 5 wt.% 10 wt.% | Unreacted TiB ₂ at low power Complete reaction at high power TiB precipitates coarser at higher filler loading Equiaxed α phase and intergranular β-phase | Increased tensile strength (after annealing/HIP) Decreased tensile strength (after annealing/HIP) Increased microhardness from 340 HV to 750 HV Increased wear resistance, with decreased weight loss from 0.35 mm ³ to 0.008 mm ³ |
| PBF-LB: | | | | | | |
| Attar et al. [41] | Assessment of laser power Assessment of scan speed | cp-Ti | TiB ₂ particles (avg. 3.5-6 µm) | 5 wt.% | Relative density of 99.5% for optimised power/speed balance Fine eutectic TiB whiskers Refined α platelets Reduced Ti grains from 2.1 µm in width and 15.3 µm in length to 0.6 µm in width and 1.1 µm in length | Hardness of 402 HV Increased compressive yield strength and ultimate strength Decreased ductility (deformation at break) under compressive load |
| Attar et al. [86] | Different laser power for different compositions | cp-Ti | TiB ₂ particles | 1.5 wt.% | α matrix instead of α' martensite Both fine and coarse TiB Accurate lattice geometry Relative density of 99.5% | Increased compressive yield strength Decreased ductility (deformation at break) under compressive load Higher hardness than powder metallurgy samples |
| Attar et al. [87] | Constant | cp-Ti | TiB ₂ particles (avg. 3.5-6 µm) | 5 wt.% | Refined TiB precipitates with respect to cast samples Refined α grains by 0.5 with respect to cast samples TiB arranged in colonies Intragranular TiB | Comparable hardness as cast samples Similar compressive behaviour as cast samples, but higher yield strength Compressive failure dominated by microcracks Higher tensile modulus than powder metallurgy samples Comparable tensile modulus (145 GPa) as cast samples (142 GPa) |
| Batalha et al. [2] | Constant | Ti-35Nb-7Zr-5Ta | TiB ₂ particles (d ₅₀ = 4 µm) | 1 wt.% | TiB precipitates in β matrix Porosity of 98.7% Lack of fusion pores Refined β columnar-dendritic crystals More equiaxed grains from a length of 327 µm and a width of 72 µm to a length of 58 µm and a width of 49 µm | Compressive tests halted at a strain of 60% without breaking Increased compressive strength by 15% Compressive Young's modulus almost unchanged at 46 GPa |
| Cai et al. [70] | Constant after preliminary optimisation of laser power and scan speed | Ti-6Al-4V | TiB ₂ particles (d ₅₀ = 2.71 µm) | 1 wt.% 2 wt.% 3 wt.% | Nearly full density, but with presence of metallurgical and inter-layer pores Wider and deeper melt pool TiB precipitates in α-Ti matrix with traces of intergranular β-Ti Refined α-Ti laths Coarsened microstructure at higher filler loading | Increasing nanohardness and depth-sensing Young's modulus for increasing filler loading Increased nanohardness from 4.38 to 6.00 GPa Increased depth-sensing Young's modulus from 131 to 143 GPa Unstable friction period (500 s max) for any filler loading Reduced average coefficient of friction from 0.44 to 0.35 (60 N load) Reduced wear mass loss from 4.4 to 2.2 mg |

(Continued)

Table 2. Continued.

| Paper | AM parameters | Matrix | Filler | Loading | Microstructure ^(a) | Properties ^(a) |
|-------------------|--|---|---|--|---|---|
| Chen et al. [35] | Constant | cp-Ti | TiB ₂ particles (avg. 3.5-6 μm) | 5 wt.% | Fine TiB precipitates Minor traces of unreacted TiB ₂ Refined α-Ti grains from 2 μm in width and 16 μm in length to 0.5 μm in width and 1 μm in length | Increased corrosion resistance in Hank's solution |
| Dong et al. [88] | Assessment of volumetric energy density (VED) through laser power and scan speed | Modified hydrogenated-dehydrogenated (HDH) Ti | TiB ₂ particles (d ₅₀ = 1.3 μm) | 0.5 wt.% 1 wt.% 2 wt.% | For 0.5 wt.% of TiB ₂ , max. density of 99.3% at intermediate VED More equiaxed and refined α/α' laths from around 10 μm to 1.11 μm Coarsened and aggregated TiB precipitates with increasing TiB ₂ loading | Increased tensile and compressive strength with increasing TiB ₂ loading Decreased tensile and compressive plasticity with increasing TiB ₂ loading 0.5 wt.% of TiB ₂ best compromise Increased hardness from 298 HV to 411 HV |
| Patil et al. [89] | Constant (DMLS) | Ti-6Al-4V | TiB ₂ particles (avg. 11 μm) | 0.2 wt.% 0.5 wt.% 1 wt.% 1.5 wt.% 2 wt.% | Reduced density (but no clear trend on TiB ₂ loading) Reduced size of martensitic laths for increasing TiB ₂ loading Change from martensitic to bimodal structure (equiaxed α and colony α) at high TiB ₂ loading | Linear trend of increasing hardness on TiB ₂ loading Increased hardness from 383 HV to 477 HV Almost unchanged coefficient of friction Increased wear resistance |
| Singh et al. [63] | Constant | Ti-6Al-7Nb | TiB ₂ particles (<10 μm) | 1.5 wt.% 3.0 wt.% | Density > 98.5% α' martensite changed to α/α' Primary TiB as nucleation site for prior β Refined microstructure with higher filler loading Quasi-continuous network of TiB at 3 wt.% of TiB ₂ | Increased hardness from 395 HV to 569 HV Increased yield strength under compression from 1029 MPa to 1633 MPa Lower corrosion current in simulated body fluid with respect to wrought Ti-6Al-4V irrespective of TiB ₂ addition |
| Su et al. [90] | Assessment of volumetric energy density (VED) through scan speed | Ti-6Al-4V | TiB ₂ particles (3-5 μm) | 1 wt.% 3 wt.% | Higher energy density (lower speed) required for printing with higher TiB ₂ loading Increasing density of composites on increasing energy density TiB preferentially at the grain boundaries Refined Ti-6Al-4V microstructure with more TiB ₂ Coarser TiB with more TiB ₂ | For neat Ti-6Al-4V, increasing microhardness with increasing energy density For composites, increasing then decreasing microhardness with increasing energy density Increased hardness from 440.765 HV to 524.387 HV Reduced friction coefficient from 0.44 to 0.35 (at maximum energy density) Increased wear resistance |
| Zhou et al. [23] | Constant (± 3 different heat treatments after printing) | Ti-6Al-4V | TiB ₂ particles (100-200 nm) | 1.88 wt.% (corresponding to 2 vol.% TiB) | Reduced width of columnar β grains and refined α/α' laths in as-built composites Clustered TiB needles in as-built composites Changed microstructure to lamellar, bilamellar or bimodal after heat treatment TiB migration to molten pool boundaries in lamellar and bilamellar microstructures Uniform distribution of TiB in bimodal microstructure | For as-built parts, increased ultimate tensile strength from 844 MPa to 1095 MPa at 400°C, and from 512 MPa to 522 MPa at 600°C (declining strengthening effect) For as-built parts, superior creep resistance of TMCs over Ti-6Al-4V (steady-state creep rate decreased from 2.72 · 10 ⁻⁶ to 1.33 · 10 ⁻⁶ s ⁻¹ and creep rupture time increased from 19.05 h to 28.52 h at 550°C/250 MPa) Increased creep resistance of TMCs after heat treatment Steady-state creep rate of bimodal microstructure lowered by 40%, and rupture time at 250 MPa increased by 29% over as-built TMC |

^aIf not otherwise stated, for each contribution the benchmark is the corresponding B-free metal matrix.

all processes that are sensitive to kinetics (solid state diffusion, for example) will be affected or restrained. This may cause deviations from the equilibrium reactions between BN and the surrounding metal matrix. Above a certain threshold of energy being delivered to the melt pool, BN dissolves (decomposes) to N and B in the liquid metal [30]. Several contributions in the literature report that a selective depletion in N occurs while printing, as confirmed by elemental analysis of the printed parts where the content of N is significantly lower than that of B despite the 1:1 molar ratio addition in BN [30,48,61]. Owing to the small atomic radius of N (0.75 Å), the remaining N rapidly diffuses away from the original BN particles [33]. The solid solubility of N in Ti is 8 wt.% at 1000°C, but it drops to 0.1 wt.% at 100°C [30]. For relatively low concentrations below 8 wt.%, it is likely that N becomes an interstitial at high temperature, and then remains entrapped as solute atoms in the matrix as a result of fast cooling [30]. However, if the concentration of N locally exceeds the solubility limit, Ti nitrides can also form. Whereas TiN would be the equilibrium product of reaction, Avila and Bandyopadhyay [19] also observed metastable Ti nitrides, such as TiN_{0.176}, in DED-LB parts loaded with either 3 or 6 wt.% of BN (cp-Ti matrix). For higher BN loadings of 5 and 15 wt.%, Ti₃N_{1.29} became the prevailing phase in the DED-LB coatings studied by Das et al. [33,37], followed by TiB and TiN (Ti-6Al-4V matrix). Since the melting point of TiN (3600°C) is higher than that of TiB, TiN is the first solid that forms from the liquid upon cooling. The remaining liquid is then depleted in N and enriched in B, and this favours the growth of TiB and out-of-equilibrium Ti nitrides [37].

Various contributions in the literature report on the presence of partly unreacted BN particles in the printed parts [30]. This may be due to the delivered energy being insufficient to complete the dissolution of BN or to inappropriate printing parameters. Otte et al. [30] noticed that, even if the energy density remains the same, the microstructure will change if the laser power and the scanning speed are increased simultaneously. In particular, the increase in melt pool temperature favours the dissolution of BN when the laser power is increased. Accordingly, Otte et al. [30,32] recommended a laser power of 180 W or higher for completing the dissolution of BN in the melt pool for PBF-LB parts with 1 wt.% of hexagonal BN nanoplatelets. However, the minimum laser power required for completing the dissolution of BN cannot be generalised, as it depends on numerous parameters, such as the BN particle size, the filler loading, the AM technology, and the printing equipment in use. Kinetic factors may also come into play, since the cooling rate may be so high

as to prematurely interrupt the reactions between BN and Ti [19]. The survival of (partly) unreacted BN particles is thus favoured in those areas, like the perimeter of each layer and the top of the part, which undergo limited thermal cycling and experience the highest cooling rate [30,48].

Papers dealing with BN as the B source in metal AM are summarised in Table 3 [19,30,32,33,37,48,61,92]. A thorough analysis of the mechanical data gathered in the last column of Table 3 can be found in Section 8.

3.3. Lanthanum hexaboride (LaB₆)

Although less common than TiB₂ and BN, other non-elemental B precursors have also been proposed in the literature, such as lanthanum hexaboride (LaB₆) [14].

Lanthanum (La) and other rare earth elements like yttrium (Y) are known to refine the grain size of Ti alloys in small concentrations [95]. An additional advantage of rare earth elements is their ability to reduce the dissolved O concentration in Ti through a 'scavenging' phenomenon [96,97], which is due to their chemical affinity to O being stronger than that of Ti [98]. Ideally, owing to the increased tolerance to O afforded by this scavenging effect, the presence of rare earth elements would enable the adoption of less expensive Ti powders for AM, as well as the advancement of printing technologies that can be operated outside of an inert gas or vacuum chamber [14].

LaB₆, like BN, has a higher laser absorption coefficient than Ti [99]. When mixed with Ti in the presence of O, LaB₆ decomposes and reacts according to [14]:



This reaction simultaneously leads to the removal of dissolved O through the formation of nanosized La₂O₃, which remains evenly distributed in the matrix, and to the formation of TiB, which refines the Ti microstructure. An example of the resulting microstructure is shown in Figure 6a.

Birmingham et al. [14] confirmed the effectiveness of LaB₆ in WAAM. LaB₆ was added within the tolerance range specified by ASTM F2924-14(2021) [39], with the concentration of each element (La and B) being lower than 0.10 wt.%. One of the most striking consequences of introducing LaB₆ was the reduced aspect ratio of the deposited bead as compared to neat Ti-6Al-4V and to Ti-6Al-4V modified with 0.05 wt.% of B. In other words, the width of the deposited bead became much narrower, while its height sensibly increased to the point that undulations and build-up instabilities occurred upon printing. Since the bead aspect ratio changed with LaB₆, but not with elemental B, it was

Table 3. Experimental contributions discussing the addition of BN to Ti and Ti alloy parts produced by AM.

| Paper | AM parameters | Matrix | Filler | Loading | Microstructure (°) | Properties (°) |
|------------------------------|---|-----------|--|------------------------|---|---|
| DED-LB: | | | | | | |
| Avila and Bandyopadhyay [19] | Specific for each composition | cp-Ti | Hexagonal BN particles (size <74 µm) | 3 wt.% 6 wt.% | Change from α' to α-Ti Growth of TiB in α-Ti matrix, with unreacted BN, TiN, and out-of-equilibrium phases (TiN _{0.176}) Coarsened microstructure after heat treatment | Reduced early-stage oxidation rate from 6.07 · 10 ⁻² mass%/min to 1.42 · 10 ⁻² mass%/min Reduced long-term oxidation rate by 50% Reduced mass loss by 35.5% Increased hardness from 157 HV _{0.2} to 585 HV _{0.2} Increased hardness after heat treatment Increased compressive yield strength by 50 from 921 MPa to 1407 MPa Increased ultimate compressive strength by 40% from 1198 MPa to 1678 MPa Slightly reduced compressive ductility Increased hardness from 342 HV to 433 HV |
| Chao et al. [48] | Constant | Ti-6Al-4V | BN nanotubes | 0.1 wt.% 0.4 wt.% | Density >99.9% Equiaxed and refined prior-β grains from 337 µm to 9 µm (width) Reduced α lath aspect ratio from >10 to 2.1 α lath thickness of 485–550 nm Retained β phase fraction of 13% Bimodal distribution of TiB (diameters of 80–250 nm vs. 33 nm) Nanosized TiB whiskers arranged at prior-β grain boundaries Some whiskers within prior-β grains Texture weakening | Increased hardness from 604 HV _{1.0} at 5 wt.% to 877 HV _{1.0} at 10 wt.% of BN Increased Young's modulus (depth-sensing indentation) from 184 GPa at 5 wt.% to 204 GPa at 10 wt.% of BN Lowest wear rate in simulated body fluid of 1.90 · 10 ⁻⁶ mm ³ /Nm for 15 wt.% of BN at 102 J/mm ² Comparable MG63 cell morphologies and proliferation on cp-Ti and composite coatings Comparable bioactivity |
| Das et al. [33] | Assessment of energy density through laser power and scan speed | Ti-6Al-4V | Hexagonal BN particles (size: 0.5–2 µm) | 5 wt.% 15 wt.% | Coating on cp-Ti free of major defects Strong interface bonding Thicker coating at 15 wt.% than at 5 wt.% of BN Flowery/dendritic TiN + fine rod-like TiB (diameter of 50–70 nm) Presence of out-of-equilibrium phases Finer precipitates at lower BN loading Finer precipitates at lower energy density | Increased hardness to 877 HV _{1.0} Increased Young's modulus (depth-sensing indentation) to 204 GPa |
| Das et al. [37] | Assessment of energy density through laser power and scan speed | Ti-6Al-4V | Hexagonal BN particles (size: 0.5–2 µm) | 5 wt.% 15 wt.% | Coating on cp-Ti free of major defects Strong interface bonding At 38 J/mm ² , increased coating thickness from 467 µm to 912 µm (but no difference in thickness at 102 J/mm ²) Flowery/dendritic TiN + fine rod-like TiB Presence of out-of-equilibrium phases Finer precipitates at lower energy density | Increased hardness to 877 HV _{1.0} Increased Young's modulus (depth-sensing indentation) to 204 GPa |
| PBF-LB: | | | | | | |
| Minasyan et al. [92] | Assessment of laser power | cp-Ti | Cubic BN particles (size: 30–70 µm) | 5 wt.% 15 wt.% | Density of 95–99% for 5 wt.% and of 93 wt.% for 15 wt.% of BN Abundant fraction of unreacted BN Weak BN-Ti bonding at low laser power | Increased hardness for increasing filler loading |
| Otte et al. [30] | Parameter optimisation (+ heat treatment) | cp-Ti | Hexagonal BN nanoplatelets (av. size: 65–75 nm; width <100 nm; thickness <10 nm) | 2.5 vol.% (ca. 1 wt.%) | Peak density of 99.67% Abundant martensitic phases Few TiB precipitates and residual BN below 140 W Refined grains After heat treatment, increased TiB diameter from 26 nm to 43 nm, and length from 5.1 µm to 17.3 µm | Increased tensile modulus by 26.5% Increased tensile yield strength by 79.2% Increased ultimate tensile strength by 57.8% Decreased ductility (deformation at break), but still higher than 5% Increased hardness by 120% |

(Continued)

Table 3. Continued.

| Paper | AM parameters | Matrix | Filler | Loading | Microstructure (°) | Properties (°) |
|------------------|--|-----------|--------------------------------------|----------|---|---|
| Otte et al. [32] | Parameter optimisation for lattice structures (+ heat treatment) | cp-Ti | BN nanoparticles (size: 65–75 nm) | 2 vol.% | Density >99%, with peak density of 99.67% Refined prior-β grains Refined α phase from coarse α grains/laths to fine acicular α TiB nanowhiskers After heat treatment, nearly equiaxed α grains of 3.6 μm After heat treatment, increased TiB diameter from 28 nm to 51 nm, and length from 5.1 μm to 16.4 μm Mixed grain structure with repeating band of columnar and equiaxed prior-β Ti grains (75 vol.% columnar) Columnar grains measuring 10 μm in width and 53 μm in length Equiaxed grains measuring 7 in size Homogeneous α laths having thickness of 0.7 μm and aspect ratio of 1.7–1.8 TiB preferentially arranged at prior-β grain boundaries | Doubled compressive yield strength of lattices to 1123 MPa Compressive modulus of 2.5 GPa (depending on porosity) Compressive strength of 62.3 MPa (depending on porosity) Elastic admissible strain of 2.5% (depending on porosity) |
| Wang et al. [61] | Constant | Ti-6Al-4V | Hexagonal BN particles (size <10 μm) | 0.5 wt.% | | Increased ultimate compressive strength from 1389 MPa to 1966 MPa Compressive yield strength of 1648 MPa Plastic strain of 6.5% Hardness of 645 HV _{0.1} in equiaxed bands Hardness of 557 HV _{0.1} in columnar bands |

^aIf not otherwise stated, for each contribution the benchmark is the corresponding B-free metal matrix.

postulated that the presence of La was the main cause for this phenomenon. By itself, La is strongly surface active. Its surface tension is lower than that of Ti, and its addition is known to reduce the liquid surface tension in many alloys. However, according to Reaction 7, La is ‘trapped’ by O while printing by WAAM, and this may drastically cut down the fraction of La that is available for modifying the surface energy of the metal alloy. Meanwhile, the same Reaction 7 drastically removes dissolved O, which is also known to decrease the surface tension in many metals. Additionally, Bermingham et al. [14] postulated that, while the surface tension of molten metals commonly decreases with increasing temperature, La might reverse the surface tension temperature coefficient of Ti-6Al-4V (according to the ‘Heiple-Roper effect’). This would reverse the Marangoni flow direction from outwards to inwards and hence hinder the melt pool from spreading laterally.

Bermingham et al. [14] also discussed the formation mechanisms of La₂O₃. Since the solubility of La is around 8 wt.% in β-Ti but nearly 0 in α-Ti, Yang et al. [100] suggested that La₂O₃ should form during the β → α transformation, and not immediately during the decomposition of LaB₆. While this mechanism is still possible, Bermingham et al. [14] backed the hypothesis that La₂O₃ should rather form while LaB₆ is decomposing. Bermingham et al. [14] noticed in fact that thermodynamic factors (Gibbs energy) would favour this scenario. Moreover, the typical cooling curves of LaB₆-modified Ti-6Al-4V acquired while printing by WAAM did not show any evidence of reactions that could correspond to the formation of La₂O₃ (or any La-containing intermetallics). Finally, Bermingham et al. [14] pointed out that La₂O₃ particles are uniformly distributed throughout the alloy in LaB₆ TMCs, which would be unlikely if La₂O₃ formed during the β → α transformation.

Similar conclusions were also reached by He et al. [99] regarding the effect of LaB₆ in Ti-6Al-4V parts produced by PBF-LB. The very fine and homogeneous distribution of La₂O₃ particles, as opposed to the segregated distribution of TiB, further confirmed the hypothesis that the decomposition of LaB₆ and the formation of La₂O₃ would be concomitant, as already proposed by Bermingham et al. [14].

Interestingly, in spite of the high laser absorption coefficient of LaB₆, He et al. [99] reported the existence of unreacted LaB₆ particles when the filler loading reached 3 wt.%. This was attributed to the tendency of LaB₆ particles to form large agglomerates at relatively high concentration. Unreacted LaB₆ particles, in their turn, became heterogeneous nucleation sites for TiB whiskers, as shown in Figure 6b.

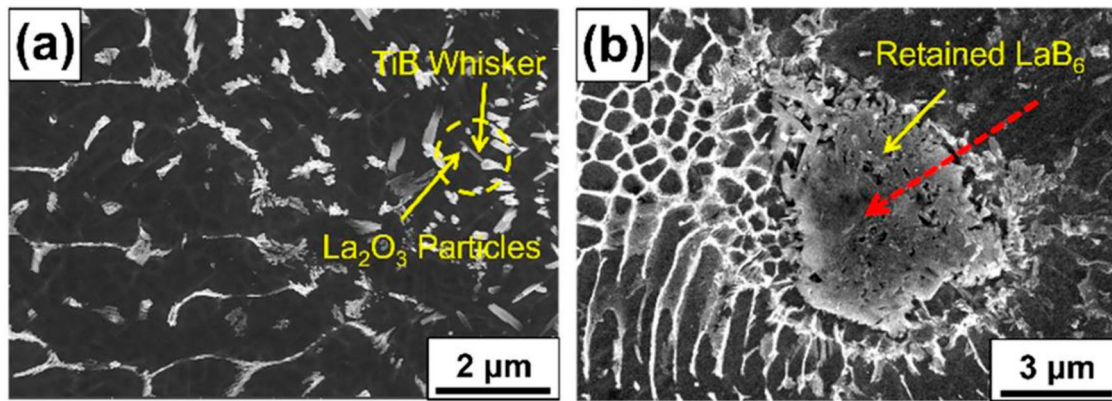


Figure 6. Scanning electron microscopy (SEM) micrographs showing the microstructure of Ti-6Al-4V samples with 3 wt.% of LaB_6 processed by PBF-LB: (a) coexistence of TiB whiskers and La_2O_3 particles, and (b) retained LaB_6 particles (pointed out by red/yellow arrows). Adapted from He et al. [99] under the Creative Commons Attribution 4.0 International (CC BY 4.0) license, <http://creativecommons.org/licenses/by/4.0/>.

Table 4 provides a summary of research papers investigating LaB_6 -modified Ti and Ti alloy parts [14,99,101]. Additional information regarding the mechanical behaviour (last column of Table 4) is given below in Section 8.

3.4. Boron carbide (B_4C)

B_4C has received great attention due to the simultaneous input of B and C that enables the formation of both TiN and TiC as highly stable and extremely hard

reinforcements. However, given its high melting point of 2350°C [102], it is very unlikely for B_4C to be fully melted/dissolved upon printing. Unmelted and unreacted B_4C particles are commonly observed even in PBF-LB, notwithstanding the highly localised energy input coming from the laser beam and the relatively high laser absorption coefficient of B_4C [103]. Another challenge in laser-based processes is represented by the low thermal diffusivity of B_4C . Although B_4C particles can efficiently absorb energy from the laser beam, they

Table 4. Experimental contributions discussing the addition of LaB_6 to Ti and Ti alloy parts produced by AM.

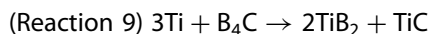
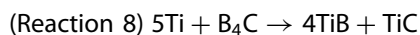
| Paper | AM parameters | Matrix | Filler | Loading | Microstructure ^(a) | Properties ^(a) |
|------------------------|---|---------------------------------|--|--|--|--|
| DED-LB: | | | | | | |
| Huang et al. (101) | Constant | β -solidifying TiAl alloy | LaB_6 nanoparticles (100 nm) | 0.2 wt.% 0.5 wt.% 1 wt.% 2 wt.% | Conversion of microstructure from nearly lamellar into duplex Reduced texture Refined β grains Reduced propensity to cracking Oxygen scavenging through La_2O_3 Ribbon-like arrangement of TiB Retained β_0 Increased porosity above 0.5 wt.% of LaB_6 | Optimised compressive properties (strength; yield strength; deformation at break) at 0.5 wt.% addition Tensile properties for 0.5 wt.% comparable to castings |
| PBF-LB: | | | | | | |
| He et al. (99) | Constant | Ti-6Al-4V | LaB_6 particles (avg. $7.4 \mu\text{m}$) | 0.5 wt.% 1 wt.% 3 wt.% | Decreased density to 96.57% Uniform distribution of La_2O_3 TiB arranged as discrete needles, then as dendritic structure, and ultimately as cell-like structure Dislocations piles up around precipitates | Increased microhardness by 35.71% Increased tensile strength by 14.5% Wear volume reduced by 47.5% Reduced ductility (deformation at break) by 37.2% |
| WAAM: | | | | | | |
| Bermingham et al. (14) | Constant (+ HIP under 150 MPa argon at 920°C for 4 h) | Ti-6Al-4V | LaB_6 , paint on build surface B, paint on build surface | Within ASTM F2924-14 (2021) limits | Reduced aspect ratio of deposited bead (by a factor of 4) and build-up instabilities Large-scale and highly oriented TiB crystals Undetectable La_2O_3 , below XRD threshold | Increased tensile strength by 10% Strongly reduced ductility Marked anisotropic effects |

^aIf not otherwise stated, for each contribution the benchmark is the corresponding B-free metal matrix.

are then unable to transfer the absorbed heat to the surrounding metal particles. If B_4C -decorated metal particles are being used as composite feedstock (an example of which is shown in Figure 7 [104]), the presence of a surface layer of B_4C may act as a thermal shield, preventing the metal from receiving energy and melting [104].

Taking into consideration its exceptional thermal stability, B_4C has been reported to dissolve in the melt pool, rather than melting. The dissolution is driven by the good compatibility between liquid Ti and B_4C , and can be described as the diffusion of B and C from (solid) B_4C into liquid Ti (or Ti alloy). In principle, Ti would also diffuse from liquid Ti into (solid) B_4C , but solid-state diffusion is much slower than liquid-state one. The dissolution of B_4C is favoured by the convective flow in the melt pool and, intuitively, complete dissolution is easier to achieve for smaller particles [103,104].

After dissolving, B_4C reacts with Ti yielding TiB (or TiB_2) and TiC as reaction products. Two reactions may occur as [105]:



However, TiB_2 is rarely observed in the literature (examples being the PBF-EB parts examined by Tao et al. [106], or the DED-LB (laser-clad) coatings analysed by Tian et al. [107]) because TiB_2 tends to react with the Ti matrix, thus leading to the formation of TiB according to Reaction 1. Moreover, according to the calculations developed by Tian et al. [107], the reaction formation enthalpy and the Gibbs free energy are negative for both reactions, but the Gibbs free energy associated with Reaction (8) is lower ('more negative') than that associated with Reaction 9 up to at least 2200 K, which indicates that TiB is likely to form in preference to TiB_2 .

Unlike TiB that grows in elongated prismatic or needle-like morphologies, TiC preferentially grows as equiaxed particles due to its bcc structure. However, dendritic structures have also been observed in C-rich areas [50,108]. Much as TiB, TiC has similar density and coefficient of thermal expansion to those of Ti, and this explains the interest towards TiC- and (TiC + TiB)-reinforced TMCs [108].

The investigation conducted by Zhang et al. [102] regarding DED-LB parts revealed a clean interface between the Ti-6Al-4V matrix and the in-situ grown TiB and TiC reinforcements, as opposed to the weak interface with the unreacted B_4C particles, which triggered

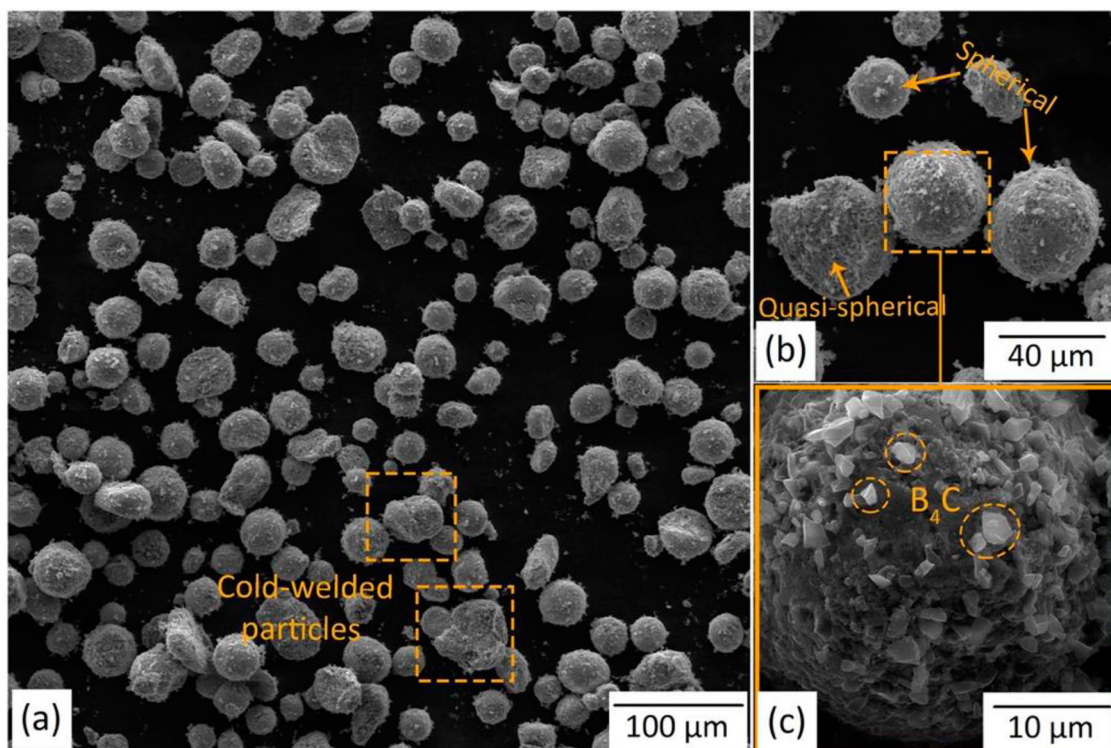


Figure 7. Scanning electron microscope (SEM) micrographs of B_4C -decorated Ti-6Al-4V powder particles obtained after 90 min of ball milling. (b) Higher magnification micrograph of (a). (c) Enclosed view of the selected region in (b). Reproduced from Fereiduni et al. [104] under the Attribution-NonCommercial-NoDerivatives 4.0 International (CC BY-NC-ND 4.0) license, <https://creativecommons.org/licenses/by-nc-nd/4.0/>.

brittle failure under tensile loading at a relatively low applied stress of 815 MPa.

In order to elucidate the role of the filler loading, Pouzet et al. [45] printed (TiB + TiC)-reinforced Ti-6Al-4V thin walls by DED-LB starting from different B₄C concentrations. The EBSD analysis of the printed parts confirmed that prior β -Ti grains were nearly equiaxed after the addition of B₄C, with a sensible reduction in grain size (d_{50}) from 150 μm for neat Ti-6Al-4V to 30 μm for the composites with 3 wt.% of B₄C. At room temperature, all samples exhibited an α/β Widmanstätten Ti matrix with TiB whiskers uniformly distributed as a network. Primary TiB prismatic crystals were also observed for the printed parts with 3 wt.% of B₄C. However, except for the sporadic formation of primary TiB precipitates, the overall microstructure was analogous for the samples with 3 wt.% of B₄C (corresponding to 2.34 wt.% B, and thus hypereutectic) and those with 1.5 wt.% of B₄C (hypoeutectic). This apparent anomaly was hypothetically explained with a shift of the Ti-B eutectic point towards higher concentration due to the high cooling rate, or with a lack of convection-aided chemical homogenisation in the melt pool. Conversely, TiC precipitates were almost undetectable, which was justified by the progressive dissolution of C in the α -phase of Ti. However, the maximum solubility of C in α -Ti was reached at 1.5 wt.% of B₄C, as demonstrated by the hardness values. Since the hardness of the printed parts was governed by C-driven solution hardening, the hardness sensibly increased when B₄C was added from 0 to 1.5 wt.%, but remained almost unchanged at 3 wt.%.

Han et al. [103] examined the effect of adding B₄C to Ti in various amount while printing by PBF-LB, also noting that the B:C atomic ratio in B₄C is 4:1, which means that the atomic concentration of B increases more rapidly than that of C as the B₄C weight fraction is being increased in the composite system. Han et al. [103] observed that adding 1 wt.% of B₄C was sufficient for changing the typical lath-type microstructure of PBF-LB Ti to a dendritic structure. As the B₄C loading increased from 2 to 5 wt.%, the microstructure further changed from dendritic to cellular hybrid. At 5 wt.% of B₄C, primary TiB crystals coexisted with nanoscale eutectic TiB + TiC structures, where TiC particles were mechanically locked on TiB whiskers. The precipitates coalesced at the grain boundaries of α -Ti and thus originated the cellular network. Meanwhile, at higher filler loadings, B₄C remained partly unreacted and large cracks were observed, which reduced the density of the printed parts and undermined the tensile strength. The highest tensile strength was thus achieved with 1 wt.% of B₄C, although this increase in strength was accompanied by a drastic drop in ductility.

Processing by an electron beam is particularly problematic due to the potential charge build-up caused by the presence of B₄C. A possible way around this consists in adding CaF₂ and other fluxes for protecting and bonding the feedstock powders. Using this system, Yun et al. [109] fabricated five TMC coatings by electron beam irradiation with different ceramic powders, including TiC, Ti + C, TiB₂, Ti + B₄C and TiC + TiB₂ powders (with CaF₂ flux being added by 50 wt.%). The comparison of the different coatings demonstrated that the composite loaded with B₄C had the highest hardness, which was preserved even at high temperature, thanks to the large volume fraction of TiB and TiC homogeneously distributed in the martensitic matrix. Similarly, Lenivtseva et al. [50] used CaF₂ (40 wt.%) and LiF (10 wt.%) to prevent oxidation in non-vacuum electron beam cladding (a technology akin electron-beam DED, DED-EB) and observed that in-situ TiB + TiC reinforced Ti claddings had improved wear resistance over cp-Ti. In order to avoid using fluxes that may evaporate and cause high voltage discharge, Tao et al. [106] pre-sintered the mixture of cp-Ti and B₄C powders by SPS, and then reprocessed the surface by PBF-EB. During the SPS pre-treatment, the temperature was kept below the minimal inter-diffusion reaction temperature between Ti and B₄C, such that a fraction of Ti particles pre-sintered without any reaction or diffusion taking place. The PBF-EB parts processed with the lowest energy input presented unreacted B₄C particles, generally surrounded by TiB₂ whiskers irradiating from the central B₄C. This peculiar microstructure was generated by the slow diffusion of B from B₄C, which favoured a local enrichment in B and thus the formation of TiB₂ instead of TiB. Afterwards, TiB₂ survived into the finished part due to fast cooling down which inhibited any further reaction with Ti. As a consequence of increasing energy input, B₄C could completely dissolve and react with Ti producing TiB whiskers and TiC particles. However, the reduced cooling rate and higher local temperature promoted the growth of coarser TiB precipitates.

The results published by Tao et al. [106] were consistent with the microstructural evolution previously described by Xia et al. [110] for PBF-LB parts, where the progressive increase in laser power and hence in energy input favoured the completion of the Ti-B₄C diffusion/reaction, but also promoted the growth of large precipitates. The main difference between the two experiments was the absence of TiB₂ crystals in the PBF-LB parts, likely due to the different convection flow and cooling rates in the melt pool.

In the contribution by Tao et al. [106], depth-sensing nanoindentation of the PBF-EB parts proved that the

samples processed at intermediate energy input achieved the highest hardness and the highest reduced elastic modulus. Likewise, the sample obtained with intermediate energy input scored the best wear resistance and the lowest coefficient of friction. The superior mechanical properties were attributed to the completion of the dissolution/reaction of B_4C , and to the growth of fine TiB precipitates [106].

Using the WAAM technique, Wang et al. [108] fabricated thin-walled parts starting from a flux-cored wire. The flux core contained a mixture of B_4C , C, Ti-6Al-4V, and Al60V40 powders, while the shell was made of pure Ti. The composition of the flux-cored wire was designed to result in a TiB + TiC fraction of either 5 wt.% or 10 wt.%, with a TiB:TiC molar ratio of 1:1. As observed by Wang et al. [108], since the solubility of B in liquid Ti is lower than that of C, the formation of TiB should precede that of TiC. However, at the ternary eutectic, the solidification sequence may be deeply affected by local fluctuations in composition, which makes it difficult to predict whether TiB, TiC, or Ti would precipitate first. The microstructural examination of the WAAM parts showed that interlaced TiB and TiC precipitates formed a three-dimensional network, which was partly discontinuous in the 5 wt.% reinforced parts and became continuous with a regular net size of around 25 μm in the 10 wt.% reinforced parts. This network was less continuous in the top layer, though, since the top layer was only melted once and did not receive additional heat input from the deposition of subsequent layers. For the same reason, the top layer also contained more pores, which were entrapped gas bubbles from the flux-cored wire. The reinforcement network was also disordered in the bottom layers, which experienced a higher cooling rate through heat conduction to the build platform. While the majority of the Ti matrix exhibited a basket-weave microstructure irrespective of the reinforcement weight fraction, the top layer had a martensitic microstructure. This suggests that Ti originally developed a martensite morphology, which was then lost upon reheating. Consistently with this hypothesis, the bottom layers had an intermediate morphology, which was the result of repeated reheating (promoting the transformation of α' martensite to other α forms) under very fast cooling rates (promoting the formation of α' martensite instead of other α forms).

Further information about experiments being conducted with B_4C is provided in Table 5 [45,50,80,102–104,106–110]. Table 5, last column, also reviews the mechanical properties of B_4C -modified parts. Additional insights into the mechanical behaviour are provided in Section 8.

4. Interaction with martensitic phases

Martensitic transformations can occur in Ti and Ti alloys as a result of fast cooling from the temperature range of β phase stability [111]. Interestingly, B may interfere with the formation of martensitic phases. In casting, it is known that B reduces the martensitic transformation temperatures of Ti. In this regard, the effect of B was demonstrated for β -Ti superelastic alloys by Horiuchi et al. [112], who observed that all the martensitic transformation temperatures of a Ti-24Nb-3Al (mol.%) alloy produced by arc melting became lower after the addition of B. In particular, the martensitic transformation start temperature, M_s , decreased linearly with the addition of B until the B concentration reached 0.05 wt.%. Above this threshold, M_s remained almost insensitive to any further B addition. Meanwhile, TiB started to form. This suggests that M_s actually depends on the concentration of B solute, such that M_s becomes progressively lower until the solubility limit of B in the β -Ti superelastic alloy is achieved at 0.05 wt.%. Above this concentration, any B addition would be rejected as TiB, with the solute concentration (and hence M_s) being unchanged.

In AM, the effect of B on martensitic phases may become more complicated due to the formation of out-of-equilibrium phases favoured by fast cooling. Quite often, Ti-6Al-4V parts produced by AM are composed of large epitaxially-grown prior- β grains containing lamellar α phase and residual intergranular β phase. The α laths are typically grouped in colonies having the same orientation. Grain boundary α also precipitates along prior- β grain boundaries [6]. On faster cooling rates, α colonies may change into a basket-weave structure (Widmanstätten). In this case, α plates nucleate on prior- β grain boundaries. However, there is not enough time for the α plates to grow across the whole grain, and new α plates start to grow from pre-existing α colonies, thus producing a sort of 'woven' microstructure [113]. An increase in cooling rate leads to a progressive refinement of the microstructure. Ultimately, if the cooling rate is high enough, Ti-6Al-4V parts may also feature α' martensite [114].

Similarly, depending on the cooling rate, cp-Ti may exhibit platelet-like α phase, or Widmanstätten structures, or finer α' martensite, or a mixture of them, with the growth of α and α' forms mainly occurring within the primary β phase. Large temperature gradients and fast cooling in AM facilitate non-equilibrium transformations and hence promote martensitic-type microstructures [115]. For this reason, α' martensite is commonly observed in cp-Ti parts processed by PBF-LB [86]. For example, Gu et al. [116] observed that cp-Ti parts

Table 5. Experimental contributions discussing the addition of B₄C to Ti and Ti alloy parts produced by AM.

| Paper | AM parameters | Matrix | Filler | Loading | Microstructure (a) | Properties (a) |
|-------------------------|---|-----------|---|--------------------------------------|--|---|
| DED-LB: | | | | | | |
| Pouzet et al. [45] | Assessment of scanning speed, laser power (and O ₂ concentration) (+ annealing at 600°C for 2 h for tensile testing) | Ti-6Al-4V | B ₄ C particles (25-45 μm) | 0.5 wt.% 1.5 wt.% 3 wt.% | Minor presence of unreacted B ₄ C Prismatic and needle-like TiB Nearly complete dissolution of C in Ti up to 1.5 wt.% of B ₄ C Equiaxed prior β-Ti Refined prior β-Ti from d ₅₀ = 150 μm to d ₅₀ = 30 μm at 3 wt.% of B ₄ C Similar microstructure for 1.5 and 3 wt.% of B ₄ C Unreacted B ₄ C surrounded by precipitates Presence of TiC, TiB (prismatic and needle-like) and traces of TiB ₂ Refined α/β-Ti phases | Similar microhardness for 1.5 wt.% (445 HV) and for 3 wt.% (455 HV) of B ₄ C Similar stiffness (dynamic resonant method) 1.5 wt.% and for 3 wt.% of B ₄ C (+10 GPa over Ti-6Al-4V at any temperature) Decreased (tensile) ductility with 1.5 wt.% of B ₄ C Brittle failure with ultimate tensile strength of 815 MPa (room temperature) |
| Zhang et al. [102] | Constant Annealing at 600°C for 2 h | Ti-6Al-4V | B ₄ C particles (30-45 μm) | 5 wt.% | Similar microstructure for 1.5 and 3 wt.% of B ₄ C Unreacted B ₄ C surrounded by precipitates Presence of TiC, TiB (prismatic and needle-like) and traces of TiB ₂ Refined α/β-Ti phases | Brittle failure with ultimate tensile strength of 815 MPa (room temperature) |
| PBF-LB: | | | | | | |
| Fereiduni et al. [104] | Assessment of volumetric energy density (VED) through laser power | Ti-6Al-4V | B ₄ C particles | 5 wt.% | Primary TiB + eutectic TiB + TiC + ternary TiB + TiC+β-Ti Evolution of β-Ti to martensitic α'-Ti Unreacted B ₄ C Dissolution of B ₄ C instead of melting | Increased microhardness by 30-30% depending on laser energy |
| Han et al. [103] | Constant after preliminary optimisation of laser power and scan speed | cp-Ti | Nanosized B ₄ C particles | 1 wt.% 2 wt.% 3 wt.% 5 wt.% | Change in microstructure from lath-type to dendritic to hybrid cellular Primary TiB + eutectic TiB + TiC TiC mechanically locked onto TiB Coalesced TiB + TiC at grain boundaries Partly unreacted B ₄ C at high filler loading Cracks at high filler loading | At 1 wt.%, increased ultimate tensile strength by 62.4%; yield strength by 49.2%; Young's modulus by 15.3% At 1 wt.%, reduced ductility (deformation at break) from 26.4% to 0.6% |
| Tian et al. [107] | Assessment of scan speed (laser surface melting) | cp-Ti | B ₄ C particles (avg: 10 μm) | 50 wt.% | TiB, TiB ₂ and TiC precipitates Coarser precipitates at slow scanning speed | Microhardness gradually decreasing towards the substrate Reduced coefficient of friction Increased wear resistance |
| Xia et al. [110] | Assessment of laser power | cp-Ti | B ₄ C particles (avg: 5 μm) | 5 wt.% | For low energy input: unreacted B ₄ C surrounded by TiB whiskers in addition to TiB and TiC For high energy input: coarse TiB | Decreasing microhardness at increasing energy input Microhardness of 577.1 HV at lowest energy |
| Xia et al. [80] | Assessment of scan speed | cp-Ti | B ₄ C particles (avg: 3 μm) | 5 wt.% | Decreased density (from 98.9% to 89.2%) and different kind of pores (prevailing lack of fusion) for increasing scan speed Coarse precipitates at low scan speed Unreacted B ₄ C | Highest microhardness of 459.3 HV at 1000 mm/s Lowest dynamic friction coefficient of 0.09 at 1400 mm/ Lowest wear rate of 0.85·10 ⁻¹³ m ³ /m at 1000 mm/s |
| Electron-beam AM | | | | | | |
| Lenitvseva et al. [50] | Assessment of beam current (power) (electron beam cladding) | cp-Ti | B ₄ C Fluxes: CaF ₂ , 40 wt.% LiF, 10 wt.% | 20 wt.% | Unreacted B ₄ C, especially in lower layers TiB whiskers TiC dendrites | Increased wear resistance especially at lowest energy input |
| Tao et al. [106] | Assessment of beam current (power) (pre-sintered specimens) | cp-Ti | B ₄ C particles (avg: 5 μm) | 4 wt.% | For low energy input: unreacted B ₄ C surrounded by TiB ₂ whiskers in addition to TiB and TiC For high energy input: coarse TiB | For intermediate energy input: highest hardness (7.75 GPa) highest reduced modulus (150.34 GPa) lowest friction coefficient (0.47) lowest wear rate (6.3 × 10 ⁻¹⁵ m ³ /Nm) |

(Continued)

Table 5. Continued.

| Paper | AM parameters | Matrix | Filler | Loading | Microstructure ^(a) | Properties ^(a) |
|-----------------------------------|--|--------------|--|--|---|---|
| Yun et al. [109] | Same for all (electron beam irradiation) | Ti-6Al-4V/Ti | B ₄ C particles (20-50 μm) + Ti particles Flux: CaF ₂ | 25 wt.% Ti-25 wt.% B ₄ C-50 wt.% CaF ₂ | Rich volume fraction of (TiB + TiC) | Highest microhardness among all TMC coatings under exam (634 HV) Retained hardness at 450°C (480 HV) |
| WAAM: Wang et al. [108] | Decreasing current for increasing number of deposited layers | Ti-6Al-4V/Ti | Flux-cored wire, core: B ₄ C, C, Ti-6Al-4V and Al60V40; shell: Ti | 5 wt.% TiB + TiC 10 wt.% TiB + TiC | Middle region: Quasi continuous network of interlaced TiB + TiC; Basket-weave prevailing morphology Top layer: less continuous network of TiB + TiC; prevailing martensite Bottom layers: intermediate microstructure between middle and top regions | Increased microhardness by 35.1% over Ti substrate Optimal wear resistance at 5 wt.% with wear loss reduced by 27.5% over non-reinforced parts |

^aIf not otherwise stated, for each contribution the benchmark is the corresponding B-free metal matrix.

processed by PBF-LB experienced a progressive change in microstructure on increasing the scan speed due to the increasing thermal and kinetic undercooling and faster solidification rate. Relatively coarse α -lath preferentially formed at relatively slow scan speed (corresponding to a high energy density), but then changed to fine acicular-shaped α' martensite, and ultimately evolved to further refined zigzag-structured α' martensite with increasing scan speed (reduced energy density).

Theoretically, α martensite may exist in two different types as hcp α' martensite or orthorhombic α'' martensite. However, the α'' type predominantly forms in β -rich alloys, while it is generally absent in cp-Ti and in $\alpha + \beta$ alloys like Ti-6Al-4V [117]. As summarised by Otte et al. [30], lath-type α' will form if the cooling rate is approximately 10^3 K s^{-1} , whereas higher cooling rates around $10^5 - 10^6 \text{ K s}^{-1}$ are required for the fine acicular α' to develop. However, it is widely acknowledged that the critical cooling rates for α' martensite to form may be affected by the composition and by the presence of impurities [118]. In AM parts, martensitic phases are preferentially located in those areas that experience limited thermal cycles, like the top layers, because subsequent reheating favours the decomposition of α' martensite to equilibrium (acicular/ Widmanstätten) α forms [6,108].

Rahman Rashid et al. [55] observed that α' -Ti needles formed in Ti-6Al-4V parts produced by DED-LB, but the microstructure changed to fine α -Ti laths after the addition of as little as 0.05 wt.% of B. According to experimental findings published by Patil et al. [89], the martensitic α' -Ti laths were gradually changed to a bimodal structure comprising equiaxed α and colony α by the progressive addition of TiB₂ in Ti-6Al-4V parts processed by PBF-LB. Interestingly, the distribution of α' martensite was discontinuous in the samples containing 0.5 wt.% of TiB₂, and α' martensite laths were selectively absent in those areas where TiB whiskers had grown. Similar results were reported for Ti-6Al-7Nb parts fabricated by PBF-LB, whose microstructure changed from α' martensite to a mixture of α and α' after the addition of TiB₂ by 1.5 wt.% (corresponding to 0.45 wt.% of B) [63].

The growth of α forms instead of α' martensite after the addition of B may have several reasons. According to Avila and Bandyopadhyay [19], the microstructural change could be attributed to the diffusion of B (or other elements, such as N, coming from non-elemental B sources) into the matrix. This may change the martensitic temperatures, as already seen in Ti castings [112]. Patil et al. [89] hypothesised that the peritectoid reaction occurring between β -Ti and TiB would produce α -Ti, rather than α' martensite. Certainly, thermal and kinetic

effects are relevant. As mentioned before, common B sources have a higher laser absorption coefficient than Ti, and therefore their presence increases the peak melt pool temperature in laser-based AM processes [37]. Additional heat energy comes from the formation reactions of TiB and other intermetallics (if present), which are exothermic [119]. Moreover, TiB and other intermetallics are refractory phases that can retain heat energy more efficiently than Ti [19]. The combination of these factors may reduce the cooling rate, lower the nucleation rate, and ultimately inhibit the formation of α' martensite. The reduction in cooling rate may be especially critical in DED-LB, which generally works with slower cooling rates than PBF-LB [120], with the typical cooling rates being in the order of 10^3 – 10^5 °C/s for DED-LB [3,57], and of 10^3 – 10^8 °C/s for PBF-LB [30,57], as mentioned above.

To sum up, although steep temperature gradients and fast cooling promote martensitic-type microstructures in AM, the presence of B may impair the formation of α' martensite due to a change in the martensitic temperatures of Ti, and due to the additional heat input.

5. Grain refinement

As historically seen for Ti casting, several contributions in the literature provide evidence of the efficacy of B, even in trace amount, in reducing the grain size of Ti and its alloys in AM. For instance, Otte et al. [32] produced cp-Ti lattice structures by PBF-LB and observed a significant refinement of the columnar prior- β grains and the formation of fine acicular α phase after the addition of 2 vol.% (≈ 0.8 wt.%) of BN. Similarly, Otte et al. [30] showed that the α' lath width in cp-Ti parts processed by PBF-LB was sensibly reduced from 1.4 μm to 300 nm with the addition of 1 wt.% of BN nanoplatelets.

The addition of B and the subsequent reactions with Ti foster numerous synergistic phenomena that are responsible for grain refinement. Primary TiB crystals (if present) in the melt pool act as heterogeneous nucleation sites for β -Ti [46]. Similarly, partly undissolved B particles, or other B-source particles, may also act as nucleants [30]. Meanwhile, the dissolution of B into the melt causes constitutional undercooling. The combined presence of nucleants and solute may explain the refinement of prior β -Ti grains according to the interdependence theory, which postulates that nucleation does not occur easily in a melt if an adequate solute is not present, while the presence of a solute by itself is not sufficient for producing grain refinement since also nucleation sites are required [121].

Upon cooling, similar to Ti casting [67], the presence of B solute in AM is known to promote a morphological change of prior β -Ti grains from globular to branched dendritic [51], and this increases the grain boundary area and hence the potential nucleation sites for the α phase [67]. As seen before, eutectic TiB nanowhiskers in the solidified TMC are also efficient nucleants for the α phase [64]. This substantially helps reduce the α phase grain size in the printed part. Moreover, TiB is preferentially located at the grain boundaries, where it prevents grain growth during re-heating via Zener pinning [19].

The solute effect of B deserves particular attention on account of its exceptionally high growth restriction factor (Q) [16,17]. The addition of foreign elements to a melt can result in grain refinement due to accelerated heterogeneous nucleation via a combination of nucleant and solute effects [122,123]. Solutes having a high Q promote a fast build-up of constitutional undercooling, which in its turn prompts a fast nucleation ahead of the advancing solidus-liquidus front and results in a smaller grain size [124]. To illustrate, the growth restriction factor, Q , is 0 for both Al and V in Ti, which means they do not exert any significant influence on grain refinement regardless of their concentration in the alloy. This justifies why additively manufactured Ti-6Al-4V parts typically show large columnar prior- β grains despite containing 10 wt.% of Al and V [6,13]. Conversely, the growth restriction factor, Q , of B in Ti has been estimated at $65C_0$, where C_0 is the B concentration in wt.% [16,17].

While the growth restriction factor, Q , depends linearly on the solute content, the grain refinement efficacy of B has been suggested to depend on its concentration in a more complicated fashion. Xue et al. [51] analysed the grain refinement induced in Ti-6Al-4V parts processed by DED-LB by the addition of B up to 0.25 wt.%. While B did promote microstructural refinement at any concentration, the grain size reduction did not correlate linearly with the B content, as the grain refinement progressed faster when the B concentration was increased from 0 to 0.08 wt.% than it did when the B concentration was increased from 0.08 wt.% to 0.25 wt.%. This observation is coherent with the saturation in grain refinement commonly reported in the literature when the B content in Ti-6Al-4V and other Ti alloy castings reaches approximately 0.10 wt.% [12,54,64]. However, contradictory results have also been published in this regard. For example, Zhang et al. [13] noticed that the size of the reconstructed β grains in Ti-6Al-4V parts processed by DED-LB kept decreasing with increasing B concentrations even up to 1 wt.% of B. According to Zhang et al. [13], these discrepancies originate from

the different cooling rates. As the cooling rate increases, the solute (B) diffusion layer ahead of the solidus/liquidus interface becomes more compressed and therefore the maximum constitutional supercooling occurs closer to the interface. This promotes more nucleation events to occur closer to the solidus/liquidus interface and, if the metal or alloy contains enough potent nucleants, this will ultimately result in smaller grains. In other terms, the solute saturation point may be higher under increasing cooling rates. However, the constitutionally supercooled zone at the solidus/liquidus interface may cease to exist under extreme cooling rates, which would actually suppress any nucleation events ahead of the solidus/liquidus interface [13].

The efficacy of B as grain refiner has also been explored for β -type alloys. For example, grain refinement in β -solidifying TiAl is a switch on/switch off phenomenon whose activation requires B being added above a critical threshold of around 0.5 at.%. However, the exact amount of B required for the switch is different for alloys with different ternary or quaternary alloying elements. Moreover, alloying with

strong boride formers, such as Ta and niobium (Nb), can increase the minimum concentration of B required for grain refinement [125]. Despite these difficulties, Huang et al. [101] recently identified the addition of B through 0.5 wt.% of LaB_6 as a promising strategy to overcoming the intrinsic brittleness of (β -solidifying) TiAl alloys in AM. The grain size progressively became smaller with increasing B concentration, which helped reduce the brittleness of the matrix. However, adding LaB_6 above 0.5 wt.% caused the agglomeration of in-situ formed precipitates, which reduced the relative density of the printed parts and hence their mechanical properties including yield strength, ultimate strength, and deformation at break under compression. Likewise, in the study conducted by Batalha et al. [2] the microstructure of a Ti-35Nb-7Zr-5Ta (TNZT) β -type alloy processed by PBF-LB was substantially changed after adding 1 wt.% of TiB_2 , as seen in Figure 8. The unmodified TNZT alloy presented large and elongated β grains stretching across several layers. Conversely, the epitaxial growth was nearly suppressed in the TiB_2 -modified parts, whose microstructure changed to

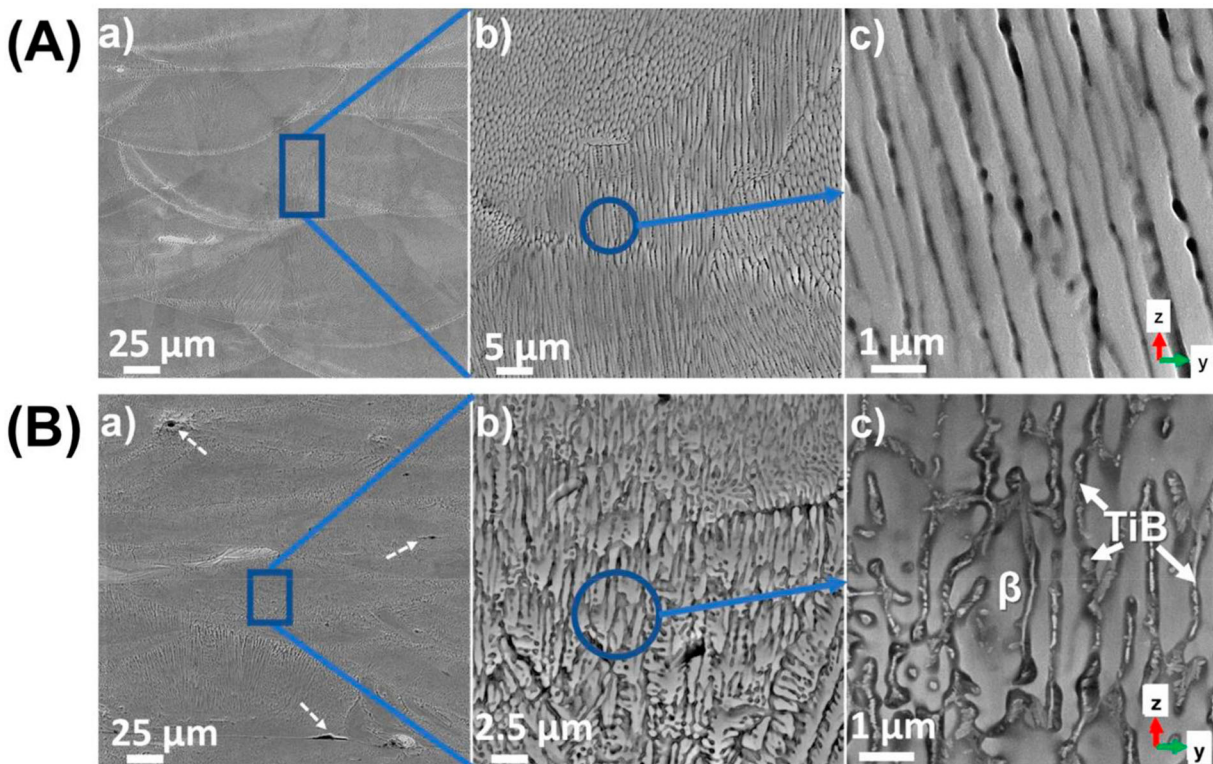


Figure 8. Scanning electron microscopy (SEM) micrographs showing the change in microstructure of a Ti-35Nb-7Zr-5Ta (TNZT) alloy processed by PBF-LB induced by the addition of 1.0 wt.% of TiB_2 . (A) Microstructure of the unmodified TNZT part: (a-c) Cellular solidification structure solely consisting of the β phase. (B) Microstructure of the TNZT part with 1 wt.% of TiB_2 : (a-c) Columnar-dendritic structure consisting of a β -Ti matrix and TiB in the interdendritic regions. The dashed arrows in (B-a) indicate lack-of-fusion-type porosity. All images were obtained with secondary electrons detector. The z-axis (red arrow) is parallel to the growth direction (adapted from Batalha et al. [2]) under the Creative Commons Attribution 4.0 International (CC BY 4.0) license, <http://creativecommons.org/licenses/by/4.0/>.

columnar-dendritic crystals. After adding B, the grain size of the TNZT parts was reduced, on average, from 327 μm to 58 μm in the growth (longitudinal) direction and from 72 μm to 49 μm in the transverse direction.

To summarise, the addition of B in trace amount is sufficient for producing a significant grain refinement of additively manufactured Ti and Ti alloy parts. Grain refinement stems from numerous interacting mechanisms, especially the strong solute effect of B. The grain refinement efficacy of B is affected by the printing conditions, since a higher cooling rate increases the solute saturation point, unless the constitutionally supercooled zone at the solidus/liquidus interface is suppressed.

6. Columnar-to-equiaxed transition

Since heat dissipation in metal AM mainly occurs parallel to the deposition (build) direction, solidification sparks from the previously deposited layers and then advances upwards. If nucleation events are not triggered ahead of the solid/liquid interface (for example, by adding heterogeneous nucleation sites), the microstructure of metal parts is thus dominated by epitaxial growth [77]. This is also very common with Ti and Ti alloys. The columnar prior- β grains can easily span across multiple layers, growing up to several millimetres in length parallel to the build direction, with a width of hundreds of microns [48]. The coarse columnar grains result in mechanical and functional property anisotropy, and reduce the ductility and the low-cycle fatigue resistance of Ti and Ti alloys [51,77].

Small additions of B may be sufficient for triggering off the CTE transition, although the degree of conversion largely depends on the AM technology in use. For example, in the PBF-LB parts fabricated by Wang et al. [61] the addition of 0.5 wt.% of BN particles to Ti-6Al-4V gave rise to a mixed grain structure with repeating bands of columnar and equiaxed prior- β grains. Xue et al. [51] noticed instead that the epitaxial growth of prior- β grains in Ti-6Al-4V parts processed by DED-LB was nearly suppressed when the concentration of B was increased from 0.08 to 0.17 wt.%. The contribution by Mahbooba et al. [82] is one of the few instances in the literature describing the effect of B on Ti-6Al-4V parts processed by electron-beam PBF (PBF-EB). Adding B and increasing its concentration from 0.25 to 0.50 wt.% gradually reduced the width of columnar prior- β grains. However, no significant changes could be observed in the prior- β grain morphology, which remained columnar. Mahbooba et al. [82] argued that the strong unidirectional heat transfer occurring in

PBF-EB still prevails over the B-induced formation of random equiaxed grains in the melt pool. Moreover, the repeated melting of layers, which is typical of PBF-EB, was identified as another potential source of directional growth, which makes prior- β grain strongly epitaxial in nature. Mahbooba et al. [82] did notice that, when the concentration of B was further increased to 1 wt.%, individual prior- β grain boundaries could not be identified in optical images. However, this is coherent with the observation made by Zhang et al. [13] that relatively high B additions eliminate grain boundary α , and this makes it very challenging to distinguish prior- β grains by optical microscopy.

Conceivably, another important variable is the B concentration. In strongly hypoeutectic systems, primary TiB particles cannot form in the melt. As a consequence, only partly unmelted B or other B-source particles (if any) are available to act as nucleants. As previously discussed, B is a powerful solute, but the grain refinement may be limited if nucleants are absent, and this may ultimately impede the CTE transition of prior- β grains [6]. Naturally, the B concentration and the printing parameters should be adjusted concomitantly, since the final microstructure is dictated by the matching between materials and processing conditions. Even with an identical chemical composition, different AM techniques or different processing conditions may result in various textures. For example, epitaxial growth may be disrupted by the deep melt pools originated by high-power DED or PBF-LB, regardless of the B concentration. It is known in fact that perturbing the Marangoni convection by controlling the energy density and thus changing the operational regime to keyhole mode can produce substantial grain refinement compared to conduction mode [126].

Since the growth of the α phase is dictated by prior- β grains (with the α phase nucleating and growing from the vicinity of prior β -Ti grain boundaries [67]), the B-induced changes to prior- β grains often result in a different morphology of the α phase at room temperature, which becomes on average smaller and more equiaxed [12,51]. Additional randomisation may occur when α phase grains are nucleated on TiB whiskers, instead of prior β grain boundaries [13]. The B-driven change in α phase microstructure was demonstrated, for example, by the DED-LB parts produced by Chao et al. [48]. The prior- β grains of neat Ti-6Al-4V parts had an average width of 337 (± 10) μm and a length of a few millimetres in the build direction. With the addition of 0.1 and 0.4 wt.% BN nanotubes, the prior β -Ti grains became uniform and equiaxed, featuring an average size of 33 and 9 μm , respectively. The highly refined prior- β grains restricted the growth of

α laths, whose aspect ratio was reduced to about 2.1, compared to >10 in the neat Ti-6Al-4V parts. Similarly, Zhang et al. [13] observed that the prior- β grain size was reduced with the progressive addition of B to Ti-6Al-4V processed by DED-LB. While the thickness of β grains exceeded 400 μm in pristine Ti-6Al-4V, β grains became smaller after the addition of 1 wt.% of B, with the maximum diameter being less than 90 μm , and were not elongated anymore along the build direction. Meanwhile, the texture intensities of the α phase were also reduced, the average α lath thickness decreased from 1.23 μm to 0.59 μm , and the presence of grain boundary α was eliminated [13]. In Ti-6Al-4V parts produced by WAAM, the width of the α laths did not sensibly change, but the length was reduced by more than fourfold when B was added by 1.3 wt.%, and this led to a corresponding reduction in aspect ratio (more equiaxed shape) [6].

Interestingly, comparable results were also described by Huo et al. [81] for high-Nb TiAl alloys processed by DED-LB. The presence of Nb, combined with fast cooling, completely eliminated the B2 (β) phase at room temperature. Meanwhile, the addition of 0.5 at.% of B led to the growth of primary TiB whiskers with a random orientation that prevented the rapid growth of large prior- β crystals, yielding a fine α phase at room temperature. As a consequence, the final microstructure consisted of very fine lamellar colonies with alternating α_2 and γ lamellae. The average size of the lamellar colony grains was reduced from 75 (no B added) to 45 μm (0.5 at.% of B). Although a complete CTE transition was not claimed, the phase transformation texture, which is an index of the lamellar orientation, was significantly lowered from 58 to 20 [81].

Even if the addition of B is generally associated with the formation of more equiaxed grains, this does not automatically imply the mitigation of anisotropic effects. For example, Birmingham et al. [14] examined the anisotropic response of Ti-6Al-4V parts fabricated by WAAM after the addition of LaB_6 in trace amount. While it was confirmed that B reduced the α -Ti grain size and largely eliminated grain boundary α , the anisotropy of the printed parts actually increased after the growth of large (>50 μm) and highly textured TiB needles that dictated a directional response under tensile loading and acted as crack initiation points.

In conclusion, B promotes the CTE transition of prior- β grains, which often leads to the formation of refined and more equiaxed α grains. Nonetheless, the prior- β grain morphology can still remain columnar in AM technologies like PBF-EB, where the strong unidirectional heat transfer and the repeated layer melting prevail on the B-induced randomisation.

Triggering the CTE transition largely depends on the interplay between B concentration and processing parameters, since primary TiB crystals in hypereutectic systems may act as nucleants and weaken the texture of the β phase, while high power DED and PBF-LB may produce deep molten pools that naturally impair epitaxial growth.

7. Densification

When it comes to the AM of TMCs, achieving fully dense parts largely depends on the appropriate adjustment of the printing parameters. Generally speaking, metallic systems containing intermetallics such as TiB (melting point of 2200°C [37]) or TiB_2 (3225°C [41]) are difficult to process, because the reinforcement melts at a much higher temperature than cp-Ti (melting point of around 1670°C [127]) and its alloys (for Ti-6Al-4V, melting in the 1604°C to 1670°C temperature range [128]). Also, the presence of the (solid state) reinforcement in the melt pool changes the dynamic viscosity of the metal matrix [41]. In PBF, tuning the processing parameters may be particularly challenging when dealing with highly porous lattice structures, because many overhanging details must be printed without support, downskin surfaces must be optimised to limit the adhesion of unmelted particles, and the perimeter of each layer becomes prevalent over the interior due to the thinness of the struts [32].

Otte et al. [30] investigated the effect of numerous combinations of laser power and hatch distance for producing fully dense parts from cp-Ti powders pre-mixed and coated with 2.5 vol% (≈ 1 wt.%) of nanosized BN platelets. As a general trend, improved densification was detected at each laser power with reducing hatch distance. Once the hatch distance was set to below 0.1 mm, the relative density of the printed parts always exceeded 99%, and the role of the laser power was almost negligible. However, as discussed above, the laser power had instead a strong effect on the advancement of the dissolution of BN in the melt and the consequent reactions with Ti.

Otte et al. [30] argued that the addition of BN by itself may be beneficial to densification, especially if BN is nanosized. Nano-BN may fill the gaps between larger Ti particles in the powder bed, and the increased bed density may favour the achievement of denser parts. Moreover, BN has a higher laser absorption coefficient than Ti [37] and a high thermal conductivity of 585 W/(m·K) (for hexagonal BN) [30]. When squeezed in between Ti (or Ti alloy) particles in the powder bed, BN would promote the interaction with the laser beam and then transfer the heat input laterally [30]. Finally,

as previously mentioned, the reactions between Ti and B are exothermic [119], thus providing an additional source of heat [30] and driving force for enhanced convection (mixing) in the melt pool [21].

Analogous considerations hold true for other B sources that, as discussed in previous sections, have a higher laser absorption coefficient than Ti, and promote exothermic reactions. Nonetheless, the formation of thermally stable intermetallics and the appearance of coarse reaction products such as primary (hypereutectic) TiB are likely to perturb the melt pool flow and its lateral spreading, which may cause microstructural defects and lower the density of the printed parts [129]. The powder-free single-track experiments conducted by He et al. [40] also suggest that the melt pool geometry in PBF-LB changes with increasing B loading, with an example being reproduced in Figure 9. After adding 1 and 2 wt.% of B to Ti-6Al-4V (where Ti-6Al-4V was chosen as the matrix due to its excellent printability), major changes in melt pool geometry only occurred in the low-power range, but for 5 and 10 wt.% of B the altered melt pool geometry extended to higher power regions. At high concentrations, normal melt pool geometries could only be observed in a narrower processing window than neat Ti-6Al-4V. This implies that the likelihood of producing defect-free parts would be lower for Ti-6Al-4V modified with a high B loading, or at least there would be less flexibility in process parameter selection.

While several authors report on the absence of any appreciable cracks in B-modified parts (for example, [24,33,37,70,85,87]), achieving parts that are free from gross defects actually requires the concurrent optimisation of filler loading and process parameters. For example, after conducting a preliminary feasibility test

that identified 167 J/m as the most convenient linear energy density for the fabrication of TMCs by LB-PBF, Han et al. [103] observed that pore- and defect-free components could only be produced when the B_4C loading was 1 wt.%, whereas micropores appeared in the specimens containing 2 and 3 wt.% of B_4C . Finally, macro-cracks formed in the TMCs loaded with 5 wt.% of B_4C , which led to a drastic drop in relative density and compromised the structural integrity of the printed parts, to the point that it was not possible to produce dumbbell-like coupons for tensile testing [103]. Likewise, He et al. [99] noticed that the laser absorption of Ti-6Al-4V increased with the addition of LaB_6 , which made printing easier. However, introducing too much LaB_6 led to metallurgical pores because the void left by the evaporation of Al could not be filled by the molten metal due to the impaired Marangoni convection. Moreover, high filler loadings caused LaB_6 particles to aggregate and become crack initiation points. Besides identifying 3 wt.% as the best filler loading that balanced off laser absorption and melt flow, He et al. [99] had to apply a high linear energy density (305.56 J/mm) to completely melt the LaB_6 particles and thus avoid cracks and other print defects.

Although often neglected in the literature, the formation of cracks upon printing is also affected by the nature of the metal matrix. While Ti and Ti-Al-6V parts are likely to crack due to the addition of ceramic particles, Huang et al. [101] were able to remediate the brittleness of a β -solidifying TiAl alloy by adding 0.5-1 wt.% of LaB_6 . Owing to the addition of LaB_6 , the coarse, nearly lamellar microstructure of the original TiAl alloy was replaced by a duplex microstructure whose fine equiaxed grains were able to accommodate strain more easily [101].

P-V: 115W-800mm/s

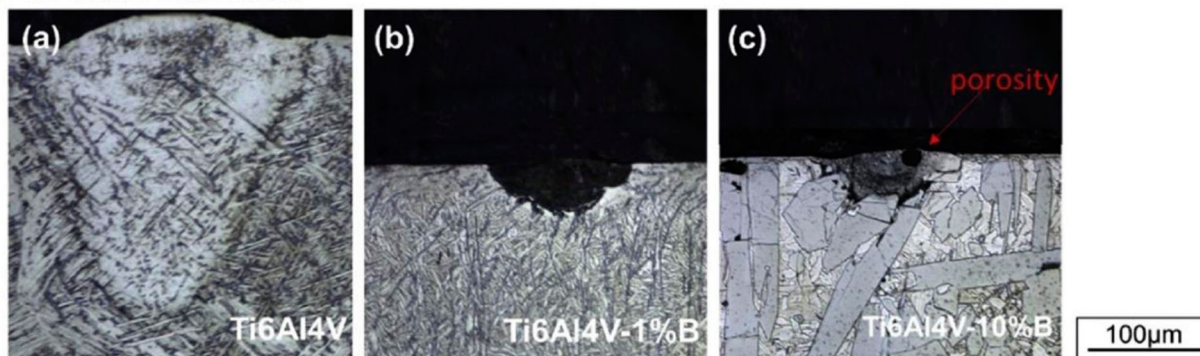


Figure 9. Change in melt pool geometry of Ti-6Al-4V caused by the addition of B in different concentration under the same processing conditions in PBF-LB (laser power: 115 W; scan speed: 800 mm/s): (a) Ti-6Al-4V, no added B; (b) Ti-6Al-4V with 1 wt.% of B; (c) Ti-6Al-4V with 10 wt.% of B. Reproduced from He et al. [40] under the Attribution-NonCommercial-NoDerivatives 4.0 International (CC BY-NC-ND 4.0) license, <https://creativecommons.org/licenses/by-nc-nd/4.0/>.

Sometimes, for a given metal-filler combination, the optimisation of the process parameters is not sufficient, and additional measures, such as pre-heating the substrate [81] or local heating after each layer deposition [108], may become necessary to eliminate cracking. Another demonstration of the difficulties associated with the AM of TiB-reinforced TMCs is given by the feasibility study published by Su et al. [90]. In this contribution, in order to assess the printability of Ti-6Al-4V parts with 1 and 3 wt.% of TiB₂ by PBF-LB (where neat Ti-6Al-4V represented the benchmark), the scan speed was progressively decreased from 1200 mm/s to 300 mm/s. With the other printing parameters being fixed, this corresponded to increasing the volumetric energy density from 104.17 J/mm³ to 416.67 J/mm³. Crack-free Ti-6Al-4V parts (no TiB₂ added) could be successfully printed as soon as the energy density reached 125 J/mm³. Conversely, the energy density required for producing crack-free components had to be increased to 250 J/mm³ for the composites with 1 wt.% of TiB₂ and finally to 416.67 J/mm³ for those with 3 wt.%. Interestingly, while the relative density of the composite parts increased with increasing energy density, the trend was the opposite for neat Ti-6Al-4V, whose density decreased with increasing energy density. Su et al. [90] suggested that Al would selectively evaporate in neat Ti-6Al-4V parts as a consequence of excessive energy input, thus leading to keyhole defects. Similarly, in one rare experiment using CrB₂ as the source of B, Kang et al. [83] observed that the density of Ti parts with 2 wt.% CrB₂ processed by PBF-LB decreased from 97.5 to 93.5% as the scan speed decreased from 1250 mm/s to 1000 mm/s. This trend was tentatively explained with the appearance of balling and dross formation at low scan speed. These defects, in turn, resulted in a poor surface quality for each new layer being built, which hampered the uniform distribution of the following powder layers.

According to Hu et al. [24], the addition of 1.6 wt.% of B caused large clusters of spherical particles to become visible on the surface of DED-LB Ti parts. Meanwhile, internal pores could also be associated to this 'balling' effect, which was attributed to poor wettability of the newly formed TiB particles. With the other printing parameters being unchanged, increasing the laser power improved the quality of the printed parts and reduced the occurrence of lack-of-fusion defects and micropores. However, despite the good correspondence of the thermodynamic behaviour of TiB and Ti, increasing the laser power (and hence the energy density) may also increase the residual stresses in the printed parts [24].

The high laser absorption coefficient of LaB₆ particles should promote the formation of a larger and deeper

melt pool [99]. However, He et al. [99] observed that the density of Ti-6Al-4V parts produced by PBF-LB decreased with the addition of LaB₆ due to the increased fraction of pores being entrapped in the melt pool by the high cooling rate. Besides the entrapped gas bubbles, the modified Marangoni convection and additional wettability issues may have contributed to the increased porosity with higher LaB₆ loading. Conversely, no pores or other defects occurred at the interface between α grains (as the main phase of the alloy matrix) and the TiB and La₂O₃ precipitates.

Residual porosity, as well as unreacted primary particles, are particularly common for B₄C-modified TMCs, likely due to the very high melting point and limited thermal diffusivity of B₄C. While increasing the beam energy may help dissolve B₄C particles and promote densification in laser-based AM, this may also induce the growth of coarse precipitates that undermine the hardness and strength of the printed parts [50,104,106,110]. Xia et al. [110] proved that decreasing the scan speed had similar effects to increasing the beam energy due to the higher energy density being delivered to the melt pool. Interestingly, the nature of the detected pores in the printed parts evolved with increasing scan speed. At low scan speed (600 mm/s, relative density of 98.9%) small spherical pores were mainly caused by gas bubbles being entrapped within the melt pool. At higher scan speed (1000 mm/s, density of 96.8%) pores became slightly larger and more elongated due to the weaker thermal convection within the melt pool. At 1400 mm/s (density of 93.5%), large and irregular pores became more frequent, as well as lack-of-fusion defects. At 1800 mm/s (density of 89.2%), the lack-of-fusion defects worsened, and the melt viscosity became too high for a proper spread of the melt pool to occur. While applying high laser power and low scanning speed may have unwanted side-effects, the size of the B₄C powders being processed is very important, because (for a given set of printing parameters) the smaller the size of the B₄C particles, the higher the chance of complete dissolution as illustrated in Figure 10 [104].

In short, most B compounds have a higher laser absorption coefficient than Ti and Ti alloys. If nano- or sub-micron-sized, B-source powders adhere to the surface of metal particles, whose increased roughness reduces laser reflection. This is expected to facilitate printing in laser-based AM technologies. Additionally, the chemical reactions occurring between B-source particles and Ti are exothermic, which improves mixing in the melt pool. Nonetheless, the addition of refractory ceramic particles generally leads to the formation of pores and cracks because of the disrupted Marangoni convection. Achieving defect-free parts requires the

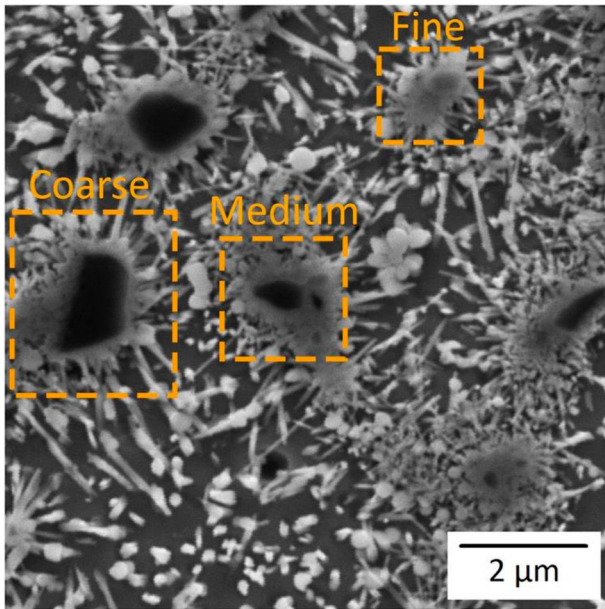


Figure 10. Scanning electron microscope (SEM) micrographs showing the effect of B_4C particle size on the dissolution progression in Ti-6Al-4V samples processed by PBF-LB under an energy density of 62.5 J/mm^3 (laser power: 250 W, scan speed: 1000 mm/s, hatch distance: 100 μm , layer thickness: 40 μm). Reproduced from Fereiduni et al. [104] under the Attribution-NonCommercial-NoDerivatives 4.0 International (CC BY-NC-ND 4.0) license, <https://creativecommons.org/licenses/by-nc-nd/4.0/>.

simultaneous optimisation of the material system composition, especially the filler concentration, and the printing parameters.

8. Mechanical properties

A NIST (National Institute of Standards and Technology) – led workshop in 2016 [130] already recognised that gaining a ‘comprehensive understanding of processing-structure-properties-performance (PSPP) relationships’ is a crucial need for enabling a wider uptake of metal AM in industry, especially in fatigue and fracture critical applications. The underpinning philosophy is that the processing conditions (namely, the appropriate matching of printing parameters and feedstock) control the (micro-)structure of the resultant material. The material structure, in its turn, governs the mechanical properties, which ultimately dictate the performance of the additively manufactured part [130]. In order to address this need, Tables 1–5 in Section 2 (elemental B) and Section 3 (other B-sources) gather information regarding the AM method, the feedstock materials (metal matrix, and filler type and loading), the resulting structure, and the related mechanical properties, as this may enable the design of new parts featuring optimised

properties for each application. Wherever possible, the corresponding mechanical properties of the base metal matrix are also provided as a term of comparison. One of the main findings from Tables 1–5 is that the addition of B typically results in a strengthening effect. For example, based on the results of depth-sensing nanoindentation tests, the addition of 0.4 wt.% of BN nanotubes was sufficient for achieving a yield strength of around 1407 MPa and an ultimate strength of around 1678 MPa, with a remarkable increase (+50% and +40%, respectively) over the neat Ti-6Al-4V counterparts produced by DED-LB [48]. Likewise, Otte et al. [30] observed that TMCs containing 2 wt.% of BN nanoplatelets reached a maximum increase in Young’s modulus of 26.5%, yield strength of 79.2% and ultimate tensile strength of 57.8% over neat cp-Ti PBF-LB parts as measured by tensile testing at room temperature.

As discussed by Zhou et al. [131], the strength increment of TMCs can be mainly attributed to two mechanisms, namely (i) Hall-Petch (boundary) strengthening, and (ii) load-bearing transformation (load-sharing or shear-lag) strengthening. Intuitively, the effective slip length of dislocations in metals is restricted by the grain size. The smaller the grain size, the shorter the slip length of dislocations [12]. As for boundary strengthening, microstructural refinement results in a shorter distance being available for dislocations to slide. This leads to an increment of the yield strength that can be estimated based on the Hall-Petch model as:

$$\Delta\sigma_{HP} = K \left(\frac{1}{\sqrt{d_2}} - \frac{1}{\sqrt{d_1}} \right) \quad (1)$$

where K is the Hall-Petch constant, and d_1 and d_2 are the average grain sizes before and after grain refinement [131].

The increment in yield strength coming from load-bearing transformation (LBT) can be estimated as.

$$\Delta\sigma_{LBT} = 0.5\sigma_{0.2m}V_R \left(\frac{l}{d} \right)_R \omega_0 \quad (2)$$

where $\sigma_{0.2m}$ is the yield strength of the metal matrix, and V_R , $(l/d)_R$ and ω_0 are the volume fraction, the aspect ratio, and the orientation factor of the reinforcement (with $\omega_0 = 0.27$ for randomly oriented nanowhiskers) [131].

In TiB-reinforced TMCs, besides the Hall-Petch effect associated with the decreased grain size of the matrix at room temperature, the fine needle-like TiB phase decorated on the grain boundaries further increases the yield strength during plastic deformation by preventing dislocation motion on the slip plane [24,51]. Although this additional term is often neglected in the literature, Hu et al. [46] also considered that the yield

strength may be increased through dislocation hardening according to

$$\Delta\sigma_{dis} = \sqrt{(\Delta\sigma_{Or})^2 + (\Delta\sigma_{th})^2 + (\Delta\sigma_{geo})^2} \quad (3)$$

where $\Delta\sigma_{Or}$ is the Orowan stress needed for a dislocation to run across an array of TiB whiskers, $\Delta\sigma_{th}$ is the stress increment caused by the thermal expansion mismatch between TiB and Ti (or Ti alloy), which is negligible, and $\Delta\sigma_{geo}$ is the stress increment caused by strain gradient effects associated with the geometrical distribution of dislocations.

The contribution to strengthening associated with each mechanism largely depends on the volume fraction of TiB, which, in turn, largely depends on the B concentration [12]. According to Dong et al. [88], as a rule of thumb, increasing the B concentration may favour the LBT (shear-lag) effect and the HP (fine-grain) effect, but may reduce the Orowan effect and hence the dislocation hardening contribution. However, regardless of the larger or smaller contribution of individual mechanisms, according to the model proposed by Li et al. [132], the total yield strength of a metal matrix composite is rather the result of the superposition of the various strengthening mechanisms, which can be expressed as.

$$\sigma_{ys} = \sigma_{0.2m} + \Delta\sigma_{HP} + \Delta\sigma_{LBT} + \Delta\sigma_{dis} \quad (4)$$

Besides the yield strength, the Vickers hardness of Ti and Ti alloys is also known to increase with the addition of B. For example, the hardness of DED-LB parts changed from around 342 HV for neat Ti-6Al-4V to around 400 HV for the composites reinforced with 0.1 wt.% of BN nanotubes and up to around 433 HV for those with 0.4 wt.% [48]. Likewise, Rahman Rashid et al. [55] observed that the hardness of DED-LB parts increased from 390–450 HV to 510–600 HV when Ti-6Al-4V was modified with just 0.05 wt.% of B (where the range of hardness values for each material is associated with a hardness gradient across the single track, with the hardness slightly increasing from the bottom to the top of the track). Similar improvements have also been recorded with cp-Ti, with the Vickers hardness of DED-LB parts increasing from 304 HV to 393 HV with the addition of 1.6 wt.% of B [62]. The change in hardness is a consequence of the increase in yield strength promoted by the addition of B, since the material can better resist to plastic deformation [19,24]. Additionally, Ti borides and other intermetallics (if present) are intrinsically much harder than the surrounding Ti matrix [21], and this may explain the common observation that both the hardness and the yield strength of B-modified Ti increase as the B content increases, but the hardness increases more

rapidly than the yield strength does [12]. As described before, if BN is used as the B source, some N is also retained in the solidified Ti matrix as solute atoms, and N is a common α stabiliser with a very strong solid solution hardening effect [48]. Likewise, the dissolution of C (which is more soluble than B) in the Ti matrix has been identified as one of the main reasons for the increased hardness of B₄C-modified parts [106]. The enhanced hardness of B-modified Ti and TMCs is generally associated with a sensible increase in wear resistance [85,89,90], unless a significant presence of unreacted particles survives in the printed part. In fact, unreacted particles are often harder than the matrix, but they can be easily detached due to weak interfacial bonding [110]. Fine and homogeneously distributed eutectic TiB whiskers generally optimise the wear resistance and should be preferred to strongly hypereutectic microstructures featuring coarse primary TiB precipitates [44]. Bermingham et al. [6] documented the occurrence of extensive twinning in Ti-6Al-4V parts deposited by WAAM when subject to compressive load. The rapid transmission of twins along coarse α colonies induced shock waves in the metal, which caused repeated stress drops (by around 30–40 MPa) as well as audible acoustic phenomena as the applied load was increased in the plastic flow region. The addition of B by 1.3 wt.% did not suppress twinning, but largely mitigated it. As a matter of fact, the presence of B prevented the formation of large colony α , which was mostly responsible for large-scale twinning transmission. The presence of borides at the grain boundaries resulting from the addition of B may have also helped to limit the rapid growth of twins.

However, as a drawback, the presence of TiB may reduce the ductility of Ti [48,62,133]. For example, Zhang et al. [13] observed that the failure mode of Ti-6Al-4V parts produced by DED-LB remained ductile when the B concentration was 0.05 wt.%, but changed to brittle when the B concentration was increased to 0.5 wt.%. TiB is very brittle, and its detrimental effect on the ductility of the composite is emphasised as the connectivity of the TiB precipitates increases at high filler loadings [6,25]. Additional disadvantages may be associated with the use of BN as the precursor for B. The ductility of the α phase (mainly in unalloyed Ti) is in fact very sensitive to the presence of interstitials, especially N [25]. TiN is also very brittle, and the growth of large TiN dendrites may trigger long and straight transgranular cracks [33]. The loss of ductility becomes critical in lattices and scaffolds, because the thin walls of porous structures are unable to accommodate the presence of stiff and brittle TiB particles [86].

Some exceptions exist in the literature which demonstrate that adding B does not always cause embrittlement. For example, as previously mentioned, the crack-prone behaviour of a brittle β -solidifying TiAl alloy was changed to crack-free thanks to the addition of an appropriate amount of LaB₆ (around 0.5 wt.%) and to the concomitant optimisation of the DED-LD parameters, which produced a fine-grained duplex microstructure [101]. However, the loss in ductility frequently associated with the growth of brittle intermetallics and with the presence of interstitials still requires attention. The structural refinement of the reinforcement (TiB and other intermetallics) is crucial to mitigating this issue [48,81,133]. Smaller particles offer a higher specific interfacial area for bonding with the matrix, and this can enhance the strengthening effect at low filler loadings. Conversely, large particles can act as inclusions, thus provoking stress concentration and premature failure at low strain. In this regard, AM generally leads to substantially smaller TiB precipitates with respect to conventional manufacturing due to the faster cooling rates [21,55,87].

However, it is worth noting that the size of TiB and other precipitates strongly depends on the interplay between printing conditions and filler loading. On the one hand, according to the solidification theory, the average size of the solidification microstructure is inversely proportional to the square root of the cooling rate. Finer microstructural features will thus be favoured by printing at low energy input with high scan speed, as this combination increases the thermal gradients near the melt zone and induces high cooling rates [33,37]. However, increasing the concentration of B increases the peak melt pool temperature due to the higher laser absorptivity of most B sources over Ti and due to the exothermic nature of the reactions occurring between B and Ti, and this will ultimately result in the formation of coarser reaction products [33,37]. It is known in fact that the growth rate, k , depends on the (absolute) operating temperature, T , according to [110]:

$$k = k_0 \exp\left(-\frac{Q_k}{2RT}\right) \quad (5)$$

where R is the gas constant, and k_0 and Q_k are the frequency factor ($17.07 \cdot 10^{-4} \text{ m/s}^{1/2}$) and activation energy (190.3 kJ/mol) of TiB, respectively [53]. Taking into account the one-dimensional growth of TiB, the length of the whisker, x , is a function of time, t , according to [110]:

$$x = k\sqrt{t} \quad (6)$$

Although the kinetics in most AM methods may sensibly deviate from equilibrium due to the high cooling rates, an increase in local temperature is still expected to speed up the growth of larger precipitates.

The shape of the reinforcement is also important, since needle- and fibre-like reinforcements with a high aspect ratio lead to an improved strengthening effect [84,133].

It has been suggested that ductility can be partly restored by increasing the relative fraction of β phase through the addition of β stabilisers such as iron (Fe), Mo, and Nb [25]. Nonetheless, as argued by Chandran and Panda [25], earlier experience with conventional manufacturing techniques, such as powder metallurgy and sintering, suggests that the aspect ratio of TiB whiskers, and hence their reinforcing effect, are strongly dependent on the nature and relative amounts of β stabilisers added to the TMC. In future, it would be interesting to ascertain whether such a dependence between β stabilisers and the aspect ratio of TiB whiskers also exists in AM parts.

Another potential drawback is that B-driven grain refinement may reduce the fracture toughness of Ti. Sen et al. [12], for example, showed that the toughness of Ti-6Al-4V castings dropped from 126 to 38 MPa·m^{1/2} after the addition of 0.4 wt.% B. Based on the morphology of the fracture surfaces, the decrease in toughness was attributed to the refined grain size of the B-modified alloy, which reduced the tortuosity of the crack path. Similarly, as documented by Zhang et al. [11], the crack propagation rate of Ti-6Al-4V parts processed by DED-LB increased after the addition of just 0.05 wt.% of B. Since the formation of TiB precipitates was negligible, the composites retained the original ductility of Ti-6Al-4V. Meanwhile, the refined microstructure and the achievement of a more equiaxed texture significantly improved the high-cycle fatigue resistance of the composites. These findings led Zhang et al. [11] to conclude that, while the fatigue crack initiation resistance in Ti-6Al-4V was improved by the addition of B due to the reduced effective slip length, the crack growth resistance of the composite was lower than that of Ti-6Al-4V, due to the smoother (less tortuous) crack propagation along the refined prior- β grain boundaries. TiB particles may also have contributed to the formation of microcracks [11].

Ultimately, the addition of B is generally associated with an increase in strength and hardness. However, the growth of intermetallic particles may reduce the ductility of TMCs. The embrittlement may be mitigated if the TiB needles are nanosized and strongly elongated (high aspect ratio). In terms of fatigue behaviour, the B-

driven grain refinement improves the crack initiation resistance, but reduces the crack growth resistance.

9. Outlook

The microstructural manipulation of Ti-based parts through the addition of B certainly paves the way for the achievement of improved additively manufactured parts with refined grain size and mitigated anisotropy. However, additional research is needed to take full advantage of the potential benefits of B-driven microstructural design.

One of the main limitations coming from the addition of B is the decreased ductility, which is worsened at high filler loading. A way around this may be enabled by the adoption of TiB-reinforced functionally graded materials (FGMs). The engineered compositional and microstructural gradient of FGMs delivers a site-specific functional response that meets non-homogeneous service requirements. Moreover, the damage and failure resistance to normal and sliding contact or to impact can be sensibly ameliorated by introducing a controlled gradient in elastic properties at the contact surface [134–136]. Presently, TiB-reinforced TCMs with a graded composition are still relatively new in the literature [43], but the idea of improving the surface properties through an appropriate compositional design, as opposed to increasing the filler loading, may deserve further attention.

Another emerging topic of research consists in combining more than one B source in the same printed parts (for example, BN and B₄C [137–139]), or a B source with a different type of additive (for example, BN and zirconium, Zr [140]). The coexistence of multiple additives enables more compositional degree of freedoms, because it leads to the formation of multiple reinforcing phases whose relative amount can be tuned through the relative filler loading of the corresponding precursors. For example, the addition of both BN and B₄C may favour the growth of Ti borides and carbides, whose relative concentration is governed through the BN and B₄C weight fractions. It is envisioned that, under optimised printing conditions, the combination of multiple reinforcements will produce synergistic effects and result is a combination of high strength, hardness, wear resistance, and high-temperature oxidation stability, thus targeting all major limitations of Ti and Ti alloys simultaneously [139].

Recently, laser remelting, which consists in scanning each layer a second time (sometimes, repeatedly) with the same printing parameters but without adding new powder, has been attracting much interest in laser-based AM as a fast and efficient ‘in-situ heat treatment’ [141]. The additional energy input has been shown to

reduce the porosity, microstructural defects, texture, and residual stresses of additively manufactured metals and alloys, including Ti-6Al-4V [142], NiTi [143], and Al alloys [144]. Remelting is less common in PBF-EB, because the entire process is conducted at high temperature. Moreover, the dual electron beam scanning required for pre-heating and melting effectively promotes in-situ annealing. Nonetheless, remelting has also been applied to PBF-EB for enhanced microstructural refinement [145]. In spite of the advantages offered by laser and electron beam remelting, to the best of the Authors’ knowledge this approach has not been applied yet to B-modified Ti parts. Given this gap in the literature, there is scope for future research, as remelting holds the potential to remediate the printing defects and porosity that may be caused by the addition of B, and to act synergistically with B towards the microstructural homogenisation of additively manufactured Ti-based parts, with clear benefits for their mechanical performance. TiB and other intermetallics are unlikely to be remelted due to their excellent thermal stability, which means that their size will remain relatively unaffected. As a result, remelting is not expected to help reduce the size of large primary TiB crystals, which is one of the main reasons for the loss in ductility commonly observed for B-functionalised parts. However, it has been predicted that remelting can promote, to some degree, the redistribution of chemical elements in parts produced from physically pre-mixed powders [146]. The prospect of exploring whether remelting could similarly improve the distribution of TiB and other intermetallic particles is an exciting one. It might even facilitate breaking down clusters that, especially at high filler loading, may act as rigid inclusions and crack initiators [99,103].

Finally, artificial intelligence (AI) is emerging as the game-changer in materials science [147], and is also enabling advancements in AM. Machine learning (ML), as a subset of AI that is able to analyse large data sets, identify relevant outputs (‘learn’), and then make informed decisions [148], is a powerful tool that is set to accelerate materials design, testing, and production [149]. Meanwhile, AI-driven robotics can provide materials scientists with automated lab assistants that revolutionise speed and scale of experimentation [150]. ML can be profitably integrated into all stages of metal AM, from part design to post-processing [151]. ML can serve to optimise the input file preparation and expedite the discovery of new printing materials [152]. Moreover, the real-time elaboration of in-situ monitoring data can identify build anomalies and counteract them, or timely interrupt the job if needed, thus limiting energy, feedstock, and time waste [153]. ML is poised to be the

long sought-after solution to the inconsistency issues and quality fluctuations that are still hindering the industrial uptake of metal AM [154]. In principle, if properly trained, ML should be capable of unveiling the laws governing the B-triggered modification of Ti-based additively manufactured parts. In this regard, it is worth mentioning that the outcome of microstructural manipulation depends just as much on the nature and concentration of the B source, as on the appropriate choice of the process parameters for a given AM technology and a given metal matrix. This dramatically multiplies the variables in play, and conventional heuristic approaches to law discovery become inadequate. Trial-and-error experiments require a substantial effort to account for both material – and processing-related parameters, and may ultimately fail to identify complex inter-dependencies. Conversely, ML is expected to manage big data, correlate diverse physical phenomena, and predict their future evolution [147], thus paving the way for the simultaneous optimisation of materials and processing. In terms of materials, ML can also assist in the assessment of new B sources. So far, the literature has been focused on a handful of chemicals yielding B, which have been chosen mainly for their apparent practicality, availability, and affordability. However, there are numerous salts and compounds that indeed contain B [155], and their utility as B sources in AM is yet to be explored. Even more so, ML is predicted to streamline research in multi-material systems, where various B sources are combined [156].

10. Conclusions

The addition of boron (B) in trace amount is known to induce grain refinement and promote the columnar-to-equiaxed (CTE) transition in titanium (Ti) castings. Moreover, the reaction between Ti and B preferentially produces TiB, which increases the otherwise poor hardness, wear performance, and oxidation resistance of Ti. Translating this knowledge to additive manufacturing (AM) paves the way for achieving refined and stronger microstructures, and also for remediating the epitaxial growth of prior- β grains typically observed in additively manufactured Ti and Ti alloys. Theoretically, B-driven microstructural modifications should be feasible with relatively low B additions, and this would meet the tight requirements imposed by international standards (e.g. ASTM F2924-14(2021)) on the chemistry of Ti-6Al-4V parts fabricated by powder bed fusion (PBF).

An increasing body of literature does confirm the beneficial effects of B in AM. However, microstructural evolution in AM often proceeds out of equilibrium due to steep thermal gradients and high cooling rates, and

this makes it difficult to clarify the role of B in AM. While designing B-modified Ti-based materials and alloys for AM, the following open questions should be accounted for:

- Besides the addition of B, cooling rates play a critical role in the microstructural evolution of Ti and Ti alloy. While cooling rates are typically faster in AM than in ‘conventional’ processes, sensible differences actually exist between different AM methods, with common values being 10^2 K s^{-1} for wire-arc additive manufacturing (WAAM), $10^3\text{--}10^5 \text{ K s}^{-1}$ for laser-based directed energy deposition (DED-LB), and $10^3\text{--}10^8 \text{ K s}^{-1}$ for laser-based PBF (PBF-LB). For the same AM technique, cooling rates largely depend on the specific printing parameters applied. As a consequence, results are hardly comparable across the literature.
- According to the Ti-B equilibrium phase binary diagram, the eutectic composition corresponds to 1.6 wt.% of B. However, many contributions in the literature provide evidence of a shift of the eutectic point occurring in AM. Interestingly, this shift may be towards higher or lower B concentration depending on the cooling rate and, even more so, depending on the effectiveness of Marangoni convection in redistributing B atoms within the melt pool.
- The shift of the eutectic point may also be affected by partial dissolution/reaction of B-source particles. If not pre-alloyed in the feedstock powder, undissolved/unreacted B particles or other B-sources are likely to survive into the printed part. If this is the case, only a fraction of the added B actually contributes to grain refinement and strengthening mechanisms. The degree of dissolution depends on the interplay of numerous parameters, but the completion of the dissolution process is typically favoured by nanometre-sized particles, high energy densities, and slow scanning speeds.
- While a saturation in the refining ability of B is generally reported at about 0.10 wt.% of B in Ti castings, it is not clear whether a similar saturation happens in AM, because contradictory results have been published for different AM techniques.
- Presently, there is no consensus on the ‘optimal’ B concentration in AM to maximise strength, wear performance, and oxidation resistance, while retaining ductility and crack growth resistance. Besides the uncertainties regarding the real eutectic point and saturation limit in AM, the results in the body of literature suggest that ultimately a trade-off should be achieved between increasing strength and hardness (favoured by high filler loadings) and preserving ductility (favoured by low filler loadings, to avoid coarse

hypereutectic TiB precipitates). It may also be questioned whether grain refinement would be enough for achieving the desired mechanical properties, or if the growth of TiB is also required.

- The literature unanimously states that B leads to grain refinement in additively manufactured Ti and Ti alloys. However, this does not automatically result in the sought-after CTE transition, especially in those AM methods that favour highly textured microstructures like electron-beam PBF (PBF-EB). A deeper understanding of B-driven microstructural changes is still needed to harness the CTE transition in a reliable and predictable way.
- In-situ grown TiB increases the hardness and wear resistance, as well as the tensile and compressive strength (both yield strength and ultimate strength) of additively manufactured Ti and Ti alloys. However, TiB is often detrimental to ductility. The embrittlement of Ti parts can be partly mitigated by the refinement of TiB precipitates. Because of faster cooling, TiB eutectic crystals are refined in AM as compared to 'conventional' manufacturing processes. However, this may be not enough for preserving the ductility of additively manufactured Ti and Ti alloys. In Ti castings, ductility can be partly restored by the addition of β stabilisers, but this may also alter the size and aspect ratio of TiB precipitates. Further investigation is needed to ascertain the feasibility of this strategy in AM.
- Future research should explore compositionally graded Ti-B systems and multi-component composites and alloys, as promising strategies for remediating the loss in ductility and for producing new multifunctional components. Attention should also be paid to in-situ remelting, which may reduce microstructural defects, improve the distribution of TiB and other intermetallics, and contribute to weakening the texture of AM Ti-based parts.
- Lastly, machine learning is expected to help elucidate the laws governing the B-driven microstructural design of Ti-based additively manufactured parts, and to streamline the combined optimisation of materials and processing parameters.

Disclosure statement

No potential conflict of interest was reported by the author(s).

Funding

AS is supported by the Commonwealth Scientific and Industrial Research Organisation (CSIRO) Research Office, Australia, through the 'Science Leader in Active Materials' platform.

ORCID

A. Sola  <http://orcid.org/0000-0002-8649-9388>

A. Trinchi  <http://orcid.org/0000-0003-0001-6566>

References

- [1] Kang L, Yang C. A review on high-strength titanium alloys: Microstructure, strengthening, and properties. *Adv Eng Mater.* 2019;21:1801359), doi:10.1002/adem.201801359
- [2] Batalha RL, Pinotti VE, Alnoaimy OOS, et al. Microstructure and properties of TiB₂-reinforced Ti-35Nb-7Zr-5Ta processed by laser-powder bed fusion. *J Mater Res.* 2022;37:259-271. doi:10.1557/s43578-021-00422-z
- [3] Ahn D-G. Directed energy deposition (DED) process: State of the art. *Int J Precis Eng Manuf-Green Technol.* 2021;8:703-742. doi:10.1007/s40684-020-00302-7
- [4] Murr LE, Gaytan SM, Ramirez DA, et al. Metal fabrication by additive manufacturing using laser and electron beam melting technologies. *J Mater Sci Technol.* 2012;28:1-14. doi:10.1016/S1005-0302(12)60016-4
- [5] Wu B, Pan Z, Ding D, et al. A review of the wire arc additive manufacturing of metals: properties, defects and quality improvement. *J Manuf Process.* 2018;35:127-139. doi:10.1016/j.jmapro.2018.08.001
- [6] Bermingham MJ, Kent D, Zhan H, et al. Controlling the microstructure and properties of wire arc additive manufactured Ti-6Al-4 V with trace boron additions. *Acta Mater.* 2015;91:289-303. doi:10.1016/j.actamat.2015.03.035
- [7] Han G, Lu X, Xia Q, et al. Face-centered-cubic titanium - A new crystal structure of Ti in a Ti-8Mo-6Fe alloy. *J Alloys Compd.* 2018;748:943-952. doi:10.1016/j.jallcom.2018.03.218
- [8] Germain L, Gey N, Humbert M. Reliability of reconstructed β -orientation maps in titanium alloys. *Ultramicroscopy.* 2007;107:1129-1135. doi:10.1016/j.ultramicro.2007.01.012
- [9] Carroll BE, Palmer TA, Beese AM. Anisotropic tensile behavior of Ti-6Al-4 V components fabricated with directed energy deposition additive manufacturing. *Acta Mater.* 2015;87:309-320. doi:10.1016/j.actamat.2014.12.054
- [10] Kok Y, Tan XP, Wang P, et al. Anisotropy and heterogeneity of microstructure and mechanical properties in metal additive manufacturing: A critical review. *Mater Des.* 2018;139:565-586. doi:10.1016/j.matdes.2017.11.021
- [11] Zhang K, Liu Y, Tian X, et al. Fatigue behaviour of L-DED processed Ti-6Al-4V with microstructures refined by trace boron addition. *Int J Fatigue.* 2023;168:107454), doi:10.1016/j.ijfatigue.2022.107454
- [12] Sen I, Tamirisakandala S, Miracle D, et al. Microstructural effects on the mechanical behavior of B-modified Ti-6Al-4 V alloys. *Acta Mater.* 2007;55:4983-4993. doi:10.1016/j.actamat.2007.05.009
- [13] Zhang K, Tian X, Bermingham M, et al. Effects of boron addition on microstructures and mechanical properties of Ti-6Al-4V manufactured by direct laser deposition. *Mater Des.* 2019;184:108191), doi:10.1016/j.matdes.2019.108191

- [14] Bermingham MJ, McDonald SD, Dargusch MS. Effect of trace lanthanum hexaboride and boron additions on microstructure, tensile properties and anisotropy of Ti-6Al-4V produced by additive manufacturing. *Mater Sci Eng A*. 2018;719:1–11. doi:10.1016/j.msea.2018.02.012
- [15] Singh G, Ramamurty U. Boron modified titanium alloys. *Prog Mater Sci*. 2020;111:100653, doi:10.1016/j.pmatsci.2020.100653
- [16] Bermingham MJ, McDonald SD, Dargusch MS, et al. Grain-refinement mechanisms in titanium alloys. *J Mater Res*. 2008;23:97–104. doi:10.1557/JMR.2008.0002
- [17] Bermingham MJ, McDonald SD, Dargusch MS, et al. The mechanism of grain refinement of titanium by silicon. *Scr Mater*. 2008;58:1050–1053. doi:10.1016/j.scriptamat.2008.01.041
- [18] Roy S, Suwas S, Tamirisakandala S, et al. Development of solidification microstructure in boron-modified alloy Ti-6Al-4V-0.1B. *Acta Mater*. 2011;59:5494–5510. doi:10.1016/j.actamat.2011.05.023
- [19] Avila JD, Bandyopadhyay A. Influence of boron nitride on reinforcement to improve high temperature oxidation resistance of titanium. *J Mater Res*. 2019;34:1279–1289. doi:10.1557/jmr.2019.11
- [20] Gorsse S, Petitcorps YL, Matar S, et al. Investigation of the Young's modulus of TiB needles in situ produced in titanium matrix composite. *Mater Sci Eng A*. 2003;340:80–87. doi:10.1016/S0921-5093(02)00188-0
- [21] Banerjee R, Genç A, Collins PC, et al. Comparison of microstructural evolution in laser-deposited and arc-melted in-situ Ti-TiB composites. *Metall Mater Trans A*. 2004;35:2143–2152. doi:10.1007/s11661-004-0162-0
- [22] Huang L, An Q, Geng L, et al. Multiscale architecture and superior high-temperature performance of discontinuously reinforced titanium matrix composites. *Adv Mater*. 2021;33:2000688, doi:10.1002/adma.202000688
- [23] Zhou Z, Liu Y, Liu X, et al. High-temperature tensile and creep properties of TiB-reinforced Ti6Al4 V composite fabricated by laser powder bed fusion. *Mater Charact*. 2023;200:112859, doi:10.1016/j.matchar.2023.112859
- [24] Hu Y, Ning F, Wang H, et al. Laser engineered net shaping of quasi-continuous network microstructural TiB reinforced titanium matrix bulk composites: Microstructure and wear performance. *Opt Laser Technol*. 2018;99:174–183. doi:10.1016/j.optlastec.2017.08.032
- [25] Chandran KSR, Panda KB. Titanium composites with TiB whiskers. *Adv Mater Process*. 2002;160:59
- [26] Koo MY, Park JS, Park MK, et al. Effect of aspect ratios of in situ formed TiB whiskers on the mechanical properties of TiBw/Ti-6Al-4 V composites. *Scr Mater*. 2012;66:487–490. doi:10.1016/j.scriptamat.2011.12.024
- [27] Morsi K, Patel VV. Processing and properties of titanium-titanium boride (TiBw) matrix composites—a review. *J Mater Sci*. 2007;42:2037–2047. doi:10.1007/s10853-006-0776-2
- [28] Tamirisakandala S, Miracle DB, Srinivasan R, et al. Titanium alloyed with boron. *Adv Mater Process*. 2006;164(12):41–43.
- [29] Wei S, Zhang Z-H, Wang F-C, et al. Effect of Ti content and sintering temperature on the microstructures and mechanical properties of TiB reinforced titanium composites synthesized by SPS process. *Mater Sci Eng A*. 2013;560:249–255. doi:10.1016/j.msea.2012.09.064
- [30] Otte JA, Zou J, Dargusch MS. High strength and ductility of titanium matrix composites by nanoscale design in selective laser melting. *J Mater Sci Technol*. 2022;118:114–127. doi:10.1016/j.jmst.2021.12.020
- [31] Tamirisakandala S, Miracle DB. Microstructure engineering of titanium alloys via small boron additions. *Int J Adv Eng Sci Appl Math*. 2010;2:168–180. doi:10.1007/s12572-011-0033-z
- [32] Otte JA, Soro N, Yang N, et al. TiB reinforced lattice structures produced by laser powder bed fusion with high elastic admissible strain. *Mater Sci Eng A*. 2022;845:143249, doi:10.1016/j.msea.2022.143249
- [33] Das M, Bhattacharya K, Dittrick SA, et al. In situ synthesized TiB-TiN reinforced Ti6Al4 V alloy composite coatings: Microstructure, tribological and in-vitro biocompatibility. *J Mech Behav Biomed Mater*. 2014;29:259–271. doi:10.1016/j.jmbbm.2013.09.006
- [34] Miklaszewski A, Jurczyk MU, Jurczyk M. Surface modification of pure titanium by TiB precipitation. *Solid State Phenom*. 2011;183:131–136. doi:10.4028/www.scientific.net/SSP.183.131
- [35] Chen Y, Zhang J, Dai N, et al. Corrosion behaviour of selective laser melted Ti-TiB biocomposite in simulated body fluid. *Electrochimica Acta*. 2017;232:89–97. doi:10.1016/j.electacta.2017.02.112
- [36] Kondoh K. Titanium metal matrix composites by powder metallurgy (PM) routes. In: Qian M, Froes F(Sam), editor. *Titan Powder Metall*. Elsevier, Butterworth-Heinemann; 2015. p. 277–297. Available from: <https://linkinghub.elsevier.com/retrieve/pii/B9780128000540000162>.
- [37] Das M, Balla VK, Basu D, et al. Laser processing of in situ synthesized TiB-TiN-reinforced Ti6Al4 V alloy coatings. *Scr Mater*. 2012;66:578–581. doi:10.1016/j.scriptamat.2012.01.010
- [38] Dadbakhsh S, Mertens R, Hao L, et al. Selective laser melting to manufacture “in situ” metal matrix composites: A review. *Adv Eng Mater*. 2019;21:1801244, doi:10.1002/adem.201801244
- [39] ASTM F2924-14(2021). Specification for additive manufacturing titanium-6 Aluminum-4 vanadium with powder bed fusion. ASTM International, F42.05 Subcommittee; 2021 [cited 2023 Apr 27]. Available from: <http://www.astm.org/cgi-bin/resolver.cgi?F2924-14R21>.
- [40] He Y, Montgomery C, Beuth J, et al. Melt pool geometry and microstructure of Ti6Al4 V with B additions processed by selective laser melting additive manufacturing. *Mater Des*. 2019;183:108126, doi:10.1016/j.matdes.2019.108126
- [41] Attar H, Bönisch M, Calin M, et al. Selective laser melting of in situ titanium-titanium boride composites: Processing, microstructure and mechanical properties. *Acta Mater*. 2014;76:13–22. doi:10.1016/j.actamat.2014.05.022
- [42] Hu Y, Ning F, Wang X, et al. Laser deposition-additive manufacturing of in situ TiB reinforced titanium matrix composites: TiB growth and part performance. *Int J Adv Manuf Technol*. 2017;93:3409–3418. doi:10.1007/s00170-017-0769-0
- [43] Shishkovsky I, Kakovkina N, Sherbakov V. Graded layered titanium composite structures with TiB₂ inclusions fabricated by selective laser melting. *Compos Struct*. 2017;169:90–96. doi:10.1016/j.compstruct.2016.11.013

- [44] Galvan D, Ocelík V, Pei Y, et al. Microstructure and properties of TiB/Ti-6Al-4V coatings produced with laser treatments. *J Mater Eng Perform.* 2004;13:406–412. doi:10.1361/10599490419919
- [45] Pouzet S, Peyre P, Gorny C, et al. Additive layer manufacturing of titanium matrix composites using the direct metal deposition laser process. *Mater Sci Eng A.* 2016;677:171–181. doi:10.1016/j.msea.2016.09.002
- [46] Hu Y, Cong W, Wang X, et al. Laser deposition-additive manufacturing of TiB-Ti composites with novel three-dimensional quasi-continuous network microstructure: Effects on strengthening and toughening. *Compos Part B Eng.* 2018;133:91–100. doi:10.1016/j.compositesb.2017.09.019
- [47] Banerjee R, Collins PC, Genç A, et al. Direct laser deposition of in situ Ti-6Al-4V-TiB composites. *Mater Sci Eng A.* 2003;358:343–349. doi:10.1016/S0921-5093(03)00299-5
- [48] Chao Q, Mateti S, Annasamy M, et al. Nanoparticle-mediated ultra grain refinement and reinforcement in additively manufactured titanium alloys. *Addit Manuf.* 2021;46:102173. doi:10.1016/j.addma.2021.102173
- [49] Kooi BJ, Pei YT, De Hosson J. The evolution of microstructure in a laser clad TiB-Ti composite coating. *Acta Mater.* 2003;51:831–845. doi:10.1016/S1359-6454(02)00475-5
- [50] Lenivtseva OG, Belousova NS, Lozhkina EA, et al. Structure and properties of Ti-C-B coatings produced by non-vacuum electron beam cladding. *IOP Conf Ser Mater Sci Eng.* 2016;156:012021. doi:10.1088/1757-899X/156/1/012021
- [51] Xue A, Lin X, Wang L, et al. Influence of trace boron addition on microstructure, tensile properties and their anisotropy of Ti6Al4 V fabricated by laser directed energy deposition. *Mater Des.* 2019;181:107943. doi:10.1016/j.matdes.2019.107943
- [52] Bhuiyan MMH, Li LH, Wang J, et al. Interfacial reactions between titanium and boron nitride nanotubes. *Scr Mater.* 2017;127:108–112. doi:10.1016/j.scriptamat.2016.09.005
- [53] Fan Z, Guo ZX, Cantor B. The kinetics and mechanism of interfacial reaction in sigma fibre-reinforced Ti MMCs. *Compos Part Appl Sci Manuf.* 1997;28:131–140. doi:10.1016/S1359-835X(96)00105-4
- [54] Tamirisakandala S, Bhat RB, Tiley JS, et al. Grain refinement of cast titanium alloys via trace boron addition. *Scr Mater.* 2005;53:1421–1426. doi:10.1016/j.scriptamat.2005.08.020
- [55] Rahman Rashid RA, Palanisamy S, Attar H, et al. Metallurgical features of direct laser-deposited Ti6Al4 V with trace boron. *J Manuf Process.* 2018;35:651–656. doi:10.1016/j.jmapro.2018.09.018
- [56] Li C, Liu ZY, Fang XY, et al. Residual stress in metal additive manufacturing. *Procedia CIRP.* 2018;71:348–353. doi:10.1016/j.procir.2018.05.039
- [57] Bermingham M, StJohn D, Easton M, et al. Revealing the mechanisms of grain nucleation and formation during additive manufacturing. *JOM.* 2020;72:1065–1073. doi:10.1007/s11837-020-04019-5
- [58] Gudur S, Nagallapati V, Pawar S, et al. A study on the effect of substrate heating and cooling on bead geometry in wire arc additive manufacturing and its correlation with cooling rate. *Mater Today Proc.* 2021;41:431–436. doi:10.1016/j.matpr.2020.10.071
- [59] Bermingham M, McDonald S, Dargusch M, et al. Microstructure of cast titanium alloys. *Mater Forum.* 2007;31:84–89.
- [60] Banerjee R, Genç A, Hill D, et al. Nanoscale TiB precipitates in laser deposited Ti-matrix composites. *Scr Mater.* 2005;53:1433–1437. doi:10.1016/j.scriptamat.2005.08.014
- [61] Wang L, Zhang Z, Zhao Z, et al. Mixed grain structure and mechanical property of Ti-6Al-4V-0.5BN (wt%) alloy fabricated by selective laser melting. *Acta Metall Sin Engl Lett.* 2023. doi:10.1007/s40195-022-01507-2
- [62] Hu Y, Zhao B, Ning F, et al. In-situ ultrafine three-dimensional quasi-continuous network microstructural TiB reinforced titanium matrix composites fabrication using laser engineered net shaping. *Mater Lett.* 2017;195:116–119. doi:10.1016/j.matlet.2017.02.112
- [63] Singh N, Acharya S, Prashanth KG, et al. Ti6Al7Nb-based TiB-reinforced composites by selective laser melting. *J Mater Res.* 2021;36:3691–3700. doi:10.1557/s43578-021-00238-x
- [64] Yang YF, Yan M, Luo SD, et al. Modification of the α -Ti laths to near equiaxed α -Ti grains in as-sintered titanium and titanium alloys by a small addition of boron. *J Alloys Compd.* 2013;579:553–557. doi:10.1016/j.jallcom.2013.07.097
- [65] Cisar JM. Titanium-boron systems. A literature survey. Knolls Atomic Power Lab. (KAPL), Niskayuna, NY (United States); 1955 [cited 2023 Apr 28]. Report No.: KAPL-M-JMC-2. Available from: <https://www.osti.gov/biblio/4346843>.
- [66] Murray JL, Liao PK, Spear KE. The B-Ti (boron-titanium) system. *Bull Alloy Phase Diagr.* 1986;7:550–555. doi:10.1007/BF02869864
- [67] Bermingham MJ, McDonald SD, Nogita K, et al. Effects of boron on microstructure in cast titanium alloys. *Scr Mater.* 2008;59:538–541. doi:10.1016/j.scriptamat.2008.05.002
- [68] Tamirisakandala S, Bhat RB, Miracle DB, et al. Effect of boron on the beta transus of Ti-6Al-4 V alloy. *Scr Mater.* 2005;53:217–222. doi:10.1016/j.scriptamat.2005.03.038
- [69] Ozerov M, Klimova M, Vyazmin A, et al. Orientation relationship in a Ti/TiB metal-matrix composite. *Mater Lett.* 2017;186:168–170. doi:10.1016/j.matlet.2016.09.124
- [70] Cai C, Radoslaw C, Zhang J, et al. In-situ preparation and formation of TiB/Ti-6Al-4V nanocomposite via laser additive manufacturing: Microstructure evolution and tribological behavior. *Powder Technol.* 2019;342:73–84. doi:10.1016/j.powtec.2018.09.088
- [71] Feng H, Zhou Y, Jia D, et al. Stacking faults formation mechanism of in situ synthesized TiB whiskers. *Scr Mater.* 2006;55:667–670. doi:10.1016/j.scriptamat.2006.07.006
- [72] Genç A, Banerjee R, Hill D, et al. Structure of TiB precipitates in laser deposited in situ, Ti-6Al-4V-TiB composites. *Mater Lett.* 2006;60:859–863. doi:10.1016/j.matlet.2005.10.033
- [73] Feng H, Zhou Y, Jia D, et al. Growth mechanism of in situ TiB whiskers in spark plasma sintered TiB/Ti metal matrix composites. *Cryst Growth Des.* 2006;6:1626–1630. doi:10.1021/cg050443k
- [74] Li DX, Ping DH, Lu YX, et al. Characterization of the microstructure in TiB-whisker reinforced Ti alloy matrix

- composite. *Mater Lett.* 1993;16:322–326. doi:10.1016/0167-577X(93)90201-8
- [75] Hill D, Banerjee R, Huber D, et al. Formation of equiaxed alpha in TiB reinforced Ti alloy composites. *Scr Mater.* 2005;52:387–392. doi:10.1016/j.scriptamat.2004.10.019
- [76] Losert W, Shi BQ, Cummins HZ. Evolution of dendritic patterns during alloy solidification: Onset of the initial instability. *Proc Natl Acad Sci USA.* 1998;95:431–438
- [77] Bermingham MJ, StJohn DH, Krynen J, et al. Promoting the columnar to equiaxed transition and grain refinement of titanium alloys during additive manufacturing. *Acta Mater.* 2019;168:261–274. doi:10.1016/j.actamat.2019.02.020
- [78] Ivasishin OM, Teliovich RV, Ivanchenko VG, et al. Processing, microstructure, texture, and tensile properties of the Ti-6Al-4V-1.55B eutectic alloy. *Metall Mater Trans A.* 2008;39:402–416. doi:10.1007/s11661-007-9425-x
- [79] Alipour S, Moridi A, Liou F, et al. The trajectory of additively manufactured titanium alloys with superior mechanical properties and engineered microstructures. *Addit Manuf.* 2022;60:103245, doi:10.1016/j.addma.2022.103245
- [80] Xia M, Liu A, Lin Y, et al. Densification behavior, microstructure evolution and fretting wear performance of in-situ hybrid strengthened Ti-based composite by laser powder-bed fusion. *Vacuum.* 2019;160:146–153. doi:10.1016/j.vacuum.2018.11.023
- [81] Huo J, He B, Lan L. Effects of boron on microstructure and mechanical properties of high-Nb TiAl alloy fabricated via laser melting deposition. *J Mater Eng Perform.* 2023. doi:10.1007/s11665-023-07851-3
- [82] Mahbooba Z, West H, Harrysson O, et al. Effect of hypoeutectic boron additions on the grain size and mechanical properties of Ti-6Al-4V manufactured with powder bed electron beam additive manufacturing. *JOM.* 2017;69:472–478. doi:10.1007/s11837-016-2210-9
- [83] Kang N, Coddet P, Liu Q, et al. In-situ TiB/near α Ti matrix composites manufactured by selective laser melting. *Addit Manuf.* 2016;11:1–6. doi:10.1016/j.addma.2016.04.001
- [84] Tjong SC, Mai Y-W. Processing-structure-property aspects of particulate- and whisker-reinforced titanium matrix composites. *Compos Sci Technol.* 2008;68:583–601. doi:10.1016/j.compscitech.2007.07.016
- [85] Wang F, Mei J, Wu X. Direct laser fabrication of Ti6Al4 V/TiB. *J Mater Process Technol.* 2008;195:321–326. doi:10.1016/j.jmatprotec.2007.05.024
- [86] Attar H, Löber L, Funk A, et al. Mechanical behavior of porous commercially pure Ti and Ti-TiB composite materials manufactured by selective laser melting. *Mater Sci Eng A.* 2015;625:350–356. doi:10.1016/j.msea.2014.12.036
- [87] Attar H, Bönisch M, Calin M, et al. Comparative study of microstructures and mechanical properties of in situ Ti-TiB composites produced by selective laser melting, powder metallurgy, and casting technologies. *J Mater Res.* 2014;29:1941–1950. doi:10.1557/jmr.2014.122
- [88] Dong Y, Li Y, Ebel T, et al. Cost-affordable, high-performance Ti-TiB composite for selective laser melting additive manufacturing. *J Mater Res.* 2020;35:1922–1935. doi:10.1557/jmr.2019.389
- [89] Patil AS, Hiwarkar VD, Verma PK, et al. Effect of TiB₂ addition on the microstructure and wear resistance of Ti-6Al-4V alloy fabricated through direct metal laser sintering (DMLS). *J Alloys Compd.* 2019;777:165–173. doi:10.1016/j.jallcom.2018.10.308
- [90] Su Y, Luo S-C, Meng L, et al. Selective laser melting of in situ TiB/Ti6Al4 V composites: formability, microstructure evolution and mechanical performance. *Acta Metall Sin Engl Lett.* 2020;33:774–788. doi:10.1007/s40195-020-01021-3
- [91] Ding ZH, Yao B, Qiu LX, et al. Formation of titanium nitride by mechanical milling and isothermal annealing of titanium and boron nitride. *J Alloys Compd.* 2005;391:77–81. doi:10.1016/j.jallcom.2004.08.051
- [92] Minasyan T, Liu L, Aydinyan S, et al. Selective laser melting of Ti/cBN composite. *Key Eng Mater.* 2019;799:257–262. doi:10.4028/www.scientific.net/KEM.799.257
- [93] Borisova AL, Borisov Y, Shvedova LK, et al. Reactions in powder Ti-BN composites. *Sov Powder Metall Met Ceram.* 1984;23:273–276. doi:10.1007/BF00796385
- [94] Gu DD, Meiners W, Wissenbach K, et al. Laser additive manufacturing of metallic components: materials, processes and mechanisms. *Int Mater Rev.* 2012;57:133–164. doi:10.1179/1743280411Y.0000000014
- [95] Samsonov GV, Kashchuk VA, Cherkashin AI. Effect of transition metals on the grain size of titanium. *Met Sci Heat Treat.* 1970;12:925–926. doi:10.1007/BF00653388
- [96] Liu Y, Liu YB, Wang B, et al. Rare earth element: Is it a necessity for PM Ti alloys? *Key Eng Mater.* 2012;520:41–48. doi:10.4028/www.scientific.net/KEM.520.41
- [97] Yan M, Tang HP, Qian M. 15 - Scavenging of oxygen and chlorine from powder metallurgy (PM) titanium and titanium alloys. In: Qian M, Froes F(Sam), editor. *Titan Powder Metall.* Elsevier, Butterworth-Heinemann; 2015. p. 253–276. Available from: <https://linkinghub.elsevier.com/retrieve/pii/B9780128000540000150>.
- [98] Yang YF, Luo SD, Qian M. The effect of lanthanum boride on the sintering, sintered microstructure and mechanical properties of titanium and titanium alloys. *Mater Sci Eng A.* 2014;618:447–455. doi:10.1016/j.msea.2014.08.080
- [99] He D, Wang H, Huang W, et al. Microstructure and mechanical properties of LaB₆/Ti-6Al-4V composites fabricated by selective laser melting. *Metals.* 2023;13:264, doi:10.3390/met13020264
- [100] Yang Z, Lu W, Zhao L, et al. Microstructure and mechanical property of in situ synthesized multiple-reinforced (TiB + TiC + La₂O₃)/Ti composites. *J Alloys Compd.* 2008;455:210–214. doi:10.1016/j.jallcom.2007.01.087
- [101] Huang D, Zhou Y, Yao X, et al. From crack-prone to crack-free: Unravelling the roles of LaB₆ in a β -solidifying TiAl alloy fabricated with laser additive manufacturing. *Mater Sci Eng A.* 2022;861:144358, doi:10.1016/j.msea.2022.144358
- [102] Zhang Y, Sun J, Vilar R. Characterization of (TiB + TiC)/TC4 in situ titanium matrix composites prepared by laser direct deposition. *J Mater Process Technol.* 2011;211:597–601. doi:10.1016/j.jmatprotec.2010.11.009
- [103] Han C, Babicheva R, Chua JDQ, et al. Microstructure and mechanical properties of (TiB + TiC)/Ti composites fabricated in situ via selective laser melting of Ti and B4C

- powders. *Addit Manuf.* 2020;36:101466), doi:10.1016/j.addma.2020.101466
- [104] Fereiduni E, Ghasemi A, Elbestawi M. Selective laser melting of hybrid ex-situ/in-situ reinforced titanium matrix composites: Laser/powder interaction, reinforcement formation mechanism, and non-equilibrium microstructural evolutions. *Mater Des.* 2019;184:108185), doi:10.1016/j.matdes.2019.108185
- [105] Tjong S, Ma ZY. Microstructural and mechanical characteristics of in situ metal matrix composites. *Mater Sci Eng R Rep.* 2000;29:49–113. doi:10.1016/S0927-796X(00)00024-3
- [106] Tao X, Yao Z, Zhang S, et al. Investigation on microstructure, mechanical and tribological properties of in-situ (TiB + TiC)/Ti composite during the electron beam surface melting. *Surf Coat Technol.* 2018;337:418–425. doi:10.1016/j.surfcoat.2018.01.054
- [107] Tian YS, Chen CZ, Chen LB, et al. Wear properties of alloyed layers produced by laser surface alloying of pure titanium with B₄C and Ti mixed powders. *J Mater Sci.* 2005;40:4387–4390. doi:10.1007/s10853-005-0736-2
- [108] Wang Z, Bai X, Que M, et al. Wire arc additive manufacturing of network microstructure (TiB + TiC)/Ti6Al4 V composites using flux-cored wires. *Ceram Int.* 2023;49:4168–4176. doi:10.1016/j.ceramint.2022.09.299
- [109] Yun E, Lee K, Lee S. Improvement of high-temperature hardness of (TiC, TiB)/Ti–6Al–4 V surface composites fabricated by high-energy electron-beam irradiation. *Surf Coat Technol.* 2004;184:74–83. doi:10.1016/j.surfcoat.2003.10.017
- [110] Xia M, Liu A, Hou Z, et al. Microstructure growth behavior and its evolution mechanism during laser additive manufacture of in-situ reinforced (TiB + TiC)/Ti composite. *J Alloys Compd.* 2017;728:436–444. doi:10.1016/j.jallcom.2017.09.033
- [111] Motyka M, Kubiak K, Sieniawski J, et al. 2.02 - Phase transformations and characterization of α + β titanium alloys. In: Hashmi S, Batalha GF, Van Tyne CJ, Yilbas B, editor. *Compr Mater Process.* Oxford: Elsevier; 2014. p. 7–36. Available from: <https://www.sciencedirect.com/science/article/pii/B9780080965321002028>.
- [112] Horiuchi Y, Inamura T, Kim HY, et al. Effect of boron concentration on martensitic transformation temperatures, stress for inducing martensite and slip stress of Ti-24 mol%Nb-3 mol%Al superelastic alloy. *Mater Trans.* 2007;48:407–413. doi:10.2320/matertrans.48.407
- [113] Gheorghe D, Pop D, Ciocoiu R, et al. Microstructure development in titanium and its alloys used for medical applications. *UPB Sci Bull Ser B Chem Mater Sci.* 2019;81:244–258
- [114] Zhong C, Liu J, Zhao T, et al. Laser metal deposition of Ti6Al4V—A brief review. *Appl Sci.* 2020;10:764), doi:10.3390/app10030764
- [115] Wysocki B, Maj P, Krawczyńska A, et al. Microstructure and mechanical properties investigation of CP titanium processed by selective laser melting (SLM). *J Mater Process Technol.* 2017;241:13–23. doi:10.1016/j.jmatprotec.2016.10.022
- [116] Gu D, Hagedorn Y-C, Meiners W, et al. Densification behavior, microstructure evolution, and wear performance of selective laser melting processed commercially pure titanium. *Acta Mater.* 2012;60:3849–3860. doi:10.1016/j.actamat.2012.04.006
- [117] Banerjee D, Williams JC. Perspectives on titanium science and technology. *Acta Mater.* 2013;61:844–879. doi:10.1016/j.actamat.2012.10.043
- [118] Oh MS, Lee J-Y, Park JK. Continuous cooling β -to- α transformation behaviors of extra-pure and commercially pure Ti. *Metall Mater Trans A.* 2004;35A:3071–3077. doi:10.1007/s11661-004-0052-5
- [119] Gordienko SP, Evtushok TM. Reaction of titanium with boron nitride under self-propagating high-temperature synthesis conditions. *Powder Metall Met Ceram.* 2001;40:58–60. doi:10.1023/A:1011359822664
- [120] DebRoy T, Wei HL, Zuback JS, et al. Additive manufacturing of metallic components – Process, structure and properties. *Prog Mater Sci.* 2018;92:112–224. doi:10.1016/j.pmatsci.2017.10.001
- [121] StJohn DH, Qian M, Easton MA, et al. The Interdependence Theory: The relationship between grain formation and nucleant selection. *Acta Mater.* 2011;59:4907–4921. doi:10.1016/j.actamat.2011.04.035
- [122] Easton M, StJohn D. Grain refinement of aluminum alloys: Part II. Confirmation of, and a mechanism for, the solute paradigm. *Metall Mater Trans A.* 1999;30:1625–1633. doi:10.1007/s11661-999-0099-4
- [123] Easton MA, StJohn DH. A model of grain refinement incorporating alloy constitution and potency of heterogeneous nucleant particles. *Acta Mater.* 2001;49:1867–1878. doi:10.1016/S1359-6454(00)00368-2
- [124] Easton MA, Qian M, Prasad A, et al. Recent advances in grain refinement of light metals and alloys. *Curr Opin Solid State Mater Sci.* 2016;20:13–24. doi:10.1016/j.cossms.2015.10.001
- [125] Cheng TT. The mechanism of grain refinement in TiAl alloys by boron addition — an alternative hypothesis. *Intermetallics.* 2000;8:29–37. doi:10.1016/S0966-9795(99)00063-1
- [126] Zhang D, Prasad A, Bermingham MJ, et al. Grain refinement of alloys in fusion-based additive manufacturing processes. *Metall Mater Trans A.* 2020;51:4341–4359. doi:10.1007/s11661-020-05880-4
- [127] Cezairliyan A, Müller AP. Melting point, normal spectral emittance (at the melting point), and electrical resistivity (above 1900K) of titanium by a pulse heating method. *J Res Natl Bur Stand.* 1977;82:119), doi:10.6028/jres.082.010
- [128] Keaveney S, Shmeliov A, Nicolosi V, et al. Investigation of process by-products during the selective laser melting of Ti6Al4 V powder. *Addit Manuf.* 2020;36:101514), doi:10.1016/j.addma.2020.101514
- [129] Essien U, Vaudreuil S. Issues in metal matrix composites fabricated by laser powder bed fusion technique: A review. *Adv Eng Mater.* 2022;24:2200055), doi:10.1002/adem.202200055
- [130] Hrabe N, Barbosa N, Daniewicz S, et al. *Findings from the NIST/ASTM workshop on mechanical behavior of additive manufacturing components.* Gaithersburg (MD): National Institute of Standards and Technology; 2016. 1–256; Report No.: NIST Advanced Manufacturing Series 100-4. Available from: <https://nvlpubs.nist.gov/nistpubs/ams/NIST.AMS.100-4.pdf>

- [131] Zhou Z, Liu Y, Liu X, et al. Microstructure evolution and mechanical properties of in-situ Ti6Al4V–TiB composites manufactured by selective laser melting. *Compos Part B Eng.* 2021;207:108567, doi:10.1016/j.compositesb.2020.108567
- [132] Li Q, Viereckl A, Rottmair CA, et al. Improved processing of carbon nanotube/magnesium alloy composites. *Compos Sci Technol.* 2009;69:1193–1199. doi:10.1016/j.compscitech.2009.02.020
- [133] Otte JA, Zou J, Huang Y, et al. Ultrahigh aspect ratio TiB nanowhisker-reinforced titanium matrix composites as lightweight and low-cost replacements for superalloys. *ACS Appl Nano Mater.* 2020;3:8208–8215. doi:10.1021/acsnanm.0c01640
- [134] Jitcharoen J, Padture NP, Giannakopoulos AE, et al. Hertzian-crack suppression in ceramics with elastic-modulus-graded surfaces. *J Am Ceram Soc.* 1998;81:2301–2308. doi:10.1111/j.1151-2916.1998.tb02625.x
- [135] Suresh S. Graded materials for resistance to contact deformation and damage. *Science.* 2001;292:2447–2451. doi:10.1126/science.1059716
- [136] Suresh S, Olsson M, Giannakopoulos AE, et al. Engineering the resistance to sliding-contact damage through controlled gradients in elastic properties at contact surfaces. *Acta Mater.* 1999;47:3915–3926. doi:10.1016/S1359-6454(99)00205-0
- [137] Traxel KD, Bandyopadhyay A. Selective laser melting of Ti6Al4V–B₄C–BN in situ reactive composites. *J Mater Res Technol.* 2022;18:2654–2671. doi:10.1016/j.jmrt.2022.03.092
- [138] Traxel KD, Bandyopadhyay A. Designing high-temperature oxidation-resistant titanium matrix composites via directed energy deposition-based additive manufacturing. *Mater Des.* 2021;212:110205, doi:10.1016/j.matdes.2021.110205
- [139] Traxel KD, Bandyopadhyay A. Influence of in situ ceramic reinforcement towards tailoring titanium matrix composites using laser-based additive manufacturing. *Addit Manuf.* 2020;31:101004, doi:10.1016/j.addma.2019.101004
- [140] Traxel KD, Bandyopadhyay A. Reactive-deposition-based additive manufacturing of Ti–Zr–BN composites. *Addit Manuf.* 2018;24:353–363. doi:10.1016/j.addma.2018.10.005
- [141] Sing SL, Yeong WY. Laser powder bed fusion for metal additive manufacturing: Perspectives on recent developments. *Virtual Phys Prototyp.* 2020;15:359–370. doi:10.1080/17452759.2020.1779999
- [142] Vaithilingam J, Goodridge RD, Hague RJM, et al. The effect of laser remelting on the surface chemistry of Ti6Al4 V components fabricated by selective laser melting. *J Mater Process Technol.* 2016;232:1–8. doi:10.1016/j.jmatprotec.2016.01.022
- [143] Bayati P, Safaei K, Nematollahi M, et al. Toward understanding the effect of remelting on the additively manufactured NiTi. *Int J Adv Manuf Technol.* 2021;112:347–360. doi:10.1007/s00170-020-06378-4
- [144] Yu W, Sing SL, Chua CK, et al. Influence of re-melting on surface roughness and porosity of AlSi10Mg parts fabricated by selective laser melting. *J Alloys Compd.* 2019;792:574–581. doi:10.1016/j.jallcom.2019.04.017
- [145] Zhang M, Zhou X, Wang D, et al. Additive manufacturing of in-situ strengthened dual-phase AlCoCuFeNi high-entropy alloy by selective electron beam melting. *J Alloys Compd.* 2022;893:162259, doi:10.1016/j.jallcom.2021.162259
- [146] Li H, Brodie EG, Hutchinson C. Predicting the chemical homogeneity in laser powder bed fusion (LPBF) of mixed powders after remelting. *Addit Manuf.* 2023;65:103447, doi:10.1016/j.addma.2023.103447
- [147] López C. Artificial intelligence and advanced materials. *Adv Mater.* 2023;35:2208683, doi:10.1002/adma.202208683
- [148] AI vs. machine learning: How do they differ?. Google Cloud. [cited 2023 Jun 12]. Available from: <https://cloud.google.com/learn/artificial-intelligence-vs-machine-learning>.
- [149] Wei J, Chu X, Sun X-Y, et al. Machine learning in materials science. *InfoMat.* 2019;1:338–358. doi:10.1002/inf2.12028
- [150] Vriza A, Chan H, Xu J. Self-driving laboratory for polymer electronics. *Chem Mater.* 2023;35:3046–3056. doi:10.1021/acs.chemmater.2c03593
- [151] Sing SL, Kuo CN, Shih CT, et al. Perspectives of using machine learning in laser powder bed fusion for metal additive manufacturing. *Virtual Phys Prototyp.* 2021;16:372–386. doi:10.1080/17452759.2021.1944229
- [152] Wang C, Tan XP, Tor SB, et al. Machine learning in additive manufacturing: State-of-the-art and perspectives. *Addit Manuf.* 2020;36:101538, doi:10.1016/j.addma.2020.101538
- [153] Herzog T, Brandt M, Trinchi A, et al. Process monitoring and machine learning for defect detection in laser-based metal additive manufacturing. *J Intell Manuf.* 2023. doi:10.1007/s10845-023-02119-y
- [154] Qin J, Hu F, Liu Y, et al. Research and application of machine learning for additive manufacturing. *Addit Manuf.* 2022;52:102691, doi:10.1016/j.addma.2022.102691
- [155] Boron and compounds - DCCEEW. [cited 2023 Jun 12]. Available from: <https://www.dcceew.gov.au/environment/protection/npisubstances/fact-sheets/boron-and-compounds#tabs-4>.
- [156] Shishkovsky I, Kakovkina N, Scherbakov V. Rapid TMC laser prototyping: compositional and phase-structural sustainability via combinatorial design of titanium-based gradient alloy reinforced by nano-sized TiC or TiB₂ ceramics. *Laser 3D Manuf V. SPIE;* 2018 [cited 2023 Jun 12]. p. 172–177. Available from: <https://www.spiedigitallibrary.org/conference-proceedings-of-spie/10523/1052315/Rapid-TMC-laser-prototyping-compositional-and-phase-structural-sustainability/10.111712.2288260.full>.